Luminescence dating estimates for the coastal MSA sequence of Hoedjiespunt 1 (South Africa)

Chantal Tribolo, Norbert Mercier, Loïc Martin, Ninon Taffin, Christopher Miller, Manuel Will, Nicholas Conard

Luminescence dating estimates for the coastal MSA sequence of Hoedjiespunt 1 (South Africa)

Tribolo Chantal[1], Mercier Norbert[1], Martin Loïc[2], Taffin Ninon[1], Miller Christopher E.[3,4,5], Will Manuel[6], Conard Nicholas[3,4,6]

1: IRAMAT-CRP2A, Université Bordeaux-Montaigne, CNRS, Pessac, France

2: Scottish Universities Environmental Research Centre, Glasgow, United Kingdom

3: Institute for Archaeological Sciences, University of Tübingen, Germany

4: Senckenberg Center for Human Evolution and Palaeoenvironment, University of Tübingen, Tübingen, Germany

5: SFF Centre for Early Sapiens Behaviour (SapienCE), University of Bergen, Norway

6: Department of Early Prehistory and Quaternary Ecology, University of Tübingen, Tübingen, Germany,

Corresponding author: ctribolo@u-bordeaux-montaigne.fr

Keyword: Middle Stone Age, luminescence dating, OSL, shell midden, coastal adaptation

Abstract: Coastal adaptations have been considered to play an important role in the bio-cultural evolution of early *Homo sapiens* and their dispersal out of Africa. In line with this assessment, recent years have seen increasing evidence for the exploitation of seafood from the Middle Stone Age (MSA) of northern and southern Africa. Yet, chronological control constitutes a key problem for better understanding the evolution of these behaviours, with little well-dated evidence for their origins in the late Middle Pleistocene and only few sites dated to before 100 ka. The shellfish-bearing MSA site of Hoedjiespunt 1 (HDP1), located in the Western Cape in South Africa, is one of the localities tentatively dated to the early Late Pleistocene. HDP1 has yielded a 1.5 m stratigraphic sequence with three phases of occupation, each containing abundant lithic artefacts, shellfish, terrestrial fauna, ostrich eggshell and pieces of ground ochre. Analyses of the cultural and zooarchaeological remains of HDP1 have provided evidence for systematic gathering of a narrow range of marine resources coupled with stable adaptations to coastal landscapes. Here we present the first complete absolute chronology for the site and its entire stratigraphic sequence by applying luminescence dating (OSL) to quartz grains extracted from the carbonate-rich sediments. The results show repeated human occupations during Marine Isotope Stages 5e-5c (~130-100 ka) at HDP1, suggesting successful integration of coastal ecosystems into the regular repertoire of behavioural adaptations by early modern humans by no later than the beginning of the Late Pleistocene.

1) Introduction

The earliest adaptations to coastal landscapes and the exploitation of seafood resources have become important topics in the past years for understanding the bio-cultural evolution of *Homo sapiens* during the Middle/Late Pleistocene (Erlandson, 2001; Parkington, 2003;

Cunnane and Stewart, 2010; Marean, 2014; Will et al., 2019). Here we employ the broad evolutionary definition of coastal adaptations that we have proposed previously (Will et al., 2016; 2019) including various behaviors such as the regular consumption and systematic acquisition of marine food resources and the expansion of settlement systems to include coastal and near-coastal zones as occupation spots on a regular and planned basis (for a similar but even broader term of coastal engagement see Faulkner et al. 2021).

Main questions of current research concern the antiquity of these behaviors (Marean et al., 2007; Jerardino and Marean 2010; Ramos-Muñoz et al., 2016) and whether *Homo sapiens* alone or also other species such as Neanderthals display these adaptations (Klein and Steele, 2008; Stringer et al., 2008; Cortés-Sánchez et al., 2011; Marean, 2014; Will et al., 2019; Zilhao et al., 2020). Further research topics include the consequences of marine food consumption for human brain evolution and demography (Crawford et al., 1999; Parkington, 2001; Broadhurst et al., 2002; Parkington, 2003, 2010; Marean, 2011; Kyriacou et al., 2014; Marean, 2016; Will et al., 2015) as well as the potential of coastal landscapes to facilitate their dispersals such as for the exit of *Homo sapiens* from Africa (Stringer, 2000; Walter et al., 2000; Mellars et al., 2013; Will et al., 2019). The wide range of topics associated with coastal adaptations and the surge of studies in the past twenty years illustrate their wider relevance in understanding early human cultural and biological evolution.

In this contribution we are particularly interested in the first of these questions, namely the age of coastal adaptations. The oldest and longest record for the consumption of marine resources derives from coastal MSA sites in northern and southern Africa with the majority of evidence coming from South Africa. The oldest currently known occurrence comes from Benzú Cave in northern Africa (~254 ka; Ramos et al., 2008; Ramos-Muñoz et al., 2016) and Pinnacle Point Cave 13B in southern Africa at ~164 ka (Jerardino and Marean, 2010; Marean et al., 2007), the only sites in Africa with potential evidence predating the Eemian interglacial. The age of these finds remains debated and the evidence for marine resource use at both sites for the late Middle Pleistocene are scant (e.g., Will et al., 2019; Tribolo, 2020). This potential MIS 8-6 evidence is followed in time by another disputed occurrence at Abdur in Eritrea dated to approximately MIS 5e (Walter et al., 2000) and more recently dated evidence at Ysterfontein 1 with the oldest ages around 120-113 ka (Niespolo et al., 2021; see also Avery et al., 2008; Klein et al., 2004). Postdating the Eemian interglacial after ~110 ka, multiple sites from South Africa show ample evidence for coastal adaptations (Fig. 1.), including on the southern coast

Klasies River (Voigt, 1973; Thackeray, 1988), Blombos Cave (Henshilwood et al., 2001; Langejans et al., 2012), Die Kelders Cave 1 (Grine et al., 1991; Marean et al., 2000), Klipdrift Shelter (Henshilwood et al., 2014) and Herolds Bay Cave (Brink and Deacon, 1982; Inskeep, 1987), and on the western coast, Ysterfontein 1 (see above), Diepkloof (Steele and Klein, 2013), Varsche Rivier 003 (Steele et al., 2016), Sea Harvest (Volman, 1978) and Hoedjiespunt 1 (HDP1; Volman, 1981; Parkington, 2003; Will et al., 2013). More recent research has shown that northern Africa likewise harbors evidence for coastal adaptations, mostly during MIS 5c-3 (Steele and Alvarez-Fernández, 2011; Dibble et al., 2012; Stoetzel et al., 2014; Campmas et al., 2016; Ramos-Muñoz et al., 2016). In Europe, while some authors have questioned the extent to what Neanderthals were adapted to coastlines and marine resources (Klein and Steele, 2008; Marean, 2014; but see Stringer et al., 2008; Zilhão et al., 2010; Cortés-Sánchez et al., 2011; Zilhao et al., 2020), there is now good evidence derived from ~30 sites distributed along the western Atlantic until eastern Mediterranean coasts in the timeframe of MIS 5-3 (see overview in Will et al., 2019). In sum, whatever the period, there is good evidence for coastal adaptations during the Late Pleistocene in sites which escaped the high sea level of the Holocene and Eemian interglacials. Yet data concerning these behaviors remain rare and disputed before ~100 ka.

Here is where the open-air site of Hoedjiespunt 1 (HDP1), located in the Western Cape of South Africa, comes into play. From a historical perspective, the site has already been known since the 1970s but only from surface collections, indicating a potential association of MSA artefacts with remains of shellfish (Volman, 1978). The first excavations that revealed the importance of HDP1 took place between 1993 and 1998, conducted by John Parkington (Parkington, 2003; Parkington et al., 2004), and mostly focused on the paleontological layers of the site (Berger and Parkington, 1995). These campaigns were followed in 2011 by fieldwork of a joint team from the University of Tübingen and the University of Cape Town directed by Nicholas Conard, exclusively in the archaeological deposits. The renewed excavations uncovered a short stratigraphic sequence of archaeological layers with *in situ* evidence for MSA stone artefacts associated with shellfish and other faunal remains (Will et al., 2013, 2015; Kyriacou et al., 2015). Crucially, HDP1 lies 15-12 meters above sea level (a.s.l.) and thus has the potential to preserve sediments predating the Eemian high sea level which was approximately 9-6 meters higher than at present in southern Africa and globally (Miller et al., 2005; Hearty et al., 2007; Carr et al., 2010).

Absolute dating of the site has, however, proven difficult so far. Initial geological age estimates by Butzer placed the site at ~70-60 ka (in Volman, 1978) with more recent work (Butzer, 2004: 1777) reiterating this placement within early MIS 4. Absolute age determinations based on OSL/IRSL (Optically stimulated luminescence/Infrared stimulated luminescence) readings of both quartz and feldspars grains from sediments, and U-series dates of ostrich eggshell from the Parkington excavations indicated a tentative age range between 130 and 100 ka for one of the archaeological horizons (AH II; Woodborne, 1999, 2000; Parkington, 2003; pers. com. from anonymous reviewer) but this was never fully confirmed and published. Based on the previous dating efforts, and in concert with stratigraphical, artefactual, faunal and contextual lines of evidence from the Conard excavations, the most recent assessment by Will *et al.* (2013; 2015) suggested an age of MIS 5e for much of the sequence. This would make HDP1 one of the oldest open-air site with good evidence for coastal adaptations in sub-Saharan Africa and provide a potential age link with the isolated MIS 6 evidence from Pinnacle Point 13B. In order to test this hypothesis and to base the absolute chronology of the site on secure evidence, however, modern dating by absolute chronometric methods is required. To this end, new sediment samples were taken from the section of the Conard excavations. In this paper, we present the ages obtained with the optically stimulated luminescence (OSL) dating method applied to quartz grains coming from nine sediment samples and discuss the further implications of these results.

2) Site and samples

The open-air locality of HDP1 lies about 110 km north-northwest of Cape Town (Fig. 1; S33°01’42”, E 17°57’34”) and is situated on the southern coast of the Hoedjiespunt Peninsula, which separates Saldana Bay from the Atlantic Ocean. The peninsula is largely composed of fossil dune deposits and in addition to several paleontological sites, also contains other archaeological localities, such as Sea Harvest, which is located about 1 km to the west (Fig. 1). HDP1 is situated in close proximity to the modern shoreline and consists of two sites: one containing archaeological materials at 15 m a.s.l., and another that is purely paleontological at 12 m a.s.l. A ~2 m thick deposit of sterile sands separates the archaeological deposits from the paleontological layers. The paleontological strata include a Middle Pleistocene hyena den

rich in fauna that yielded 14 human fossils, but no archaeology or marine shells (Berger and Parkington, 1995; Churchill et al., 2000).

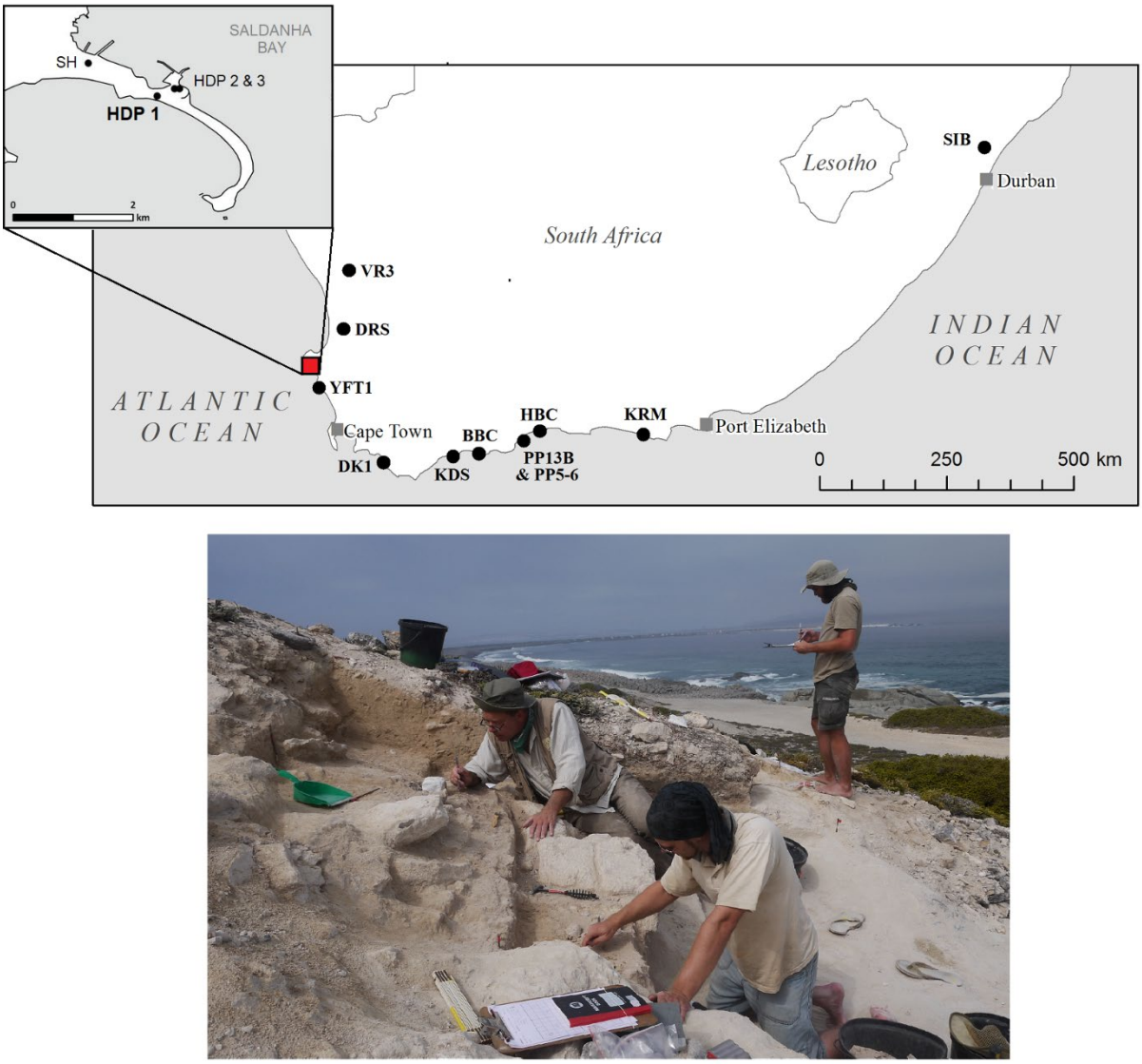

Figure 1: Location of Hoedjiespunt 1 (HDP1) in relation to other MSA sites in southern Africa (top); picture taking during the excavation of the open-air sequence of HDP1 in 2011, showing its current-day proximity to the Atlantic Ocean (bottom). Abbreviations for archaeological sites: BBC-Blombos Cave; DK1-Die Kelders 1; DRS-Diepkloof Rock Shelter; HBC-Herold´s Bay Cave; HDP1-Hoedjiespunt 1; KDS-Klipdrift Shelter; KRM-Klasies River Mouth; PP13B/PP5-6-Pinnacle Point Cave 13B & 5-6; SH-Sea Harvest; YFT1-Ysterfontein 1; SIB-Sibhudu; VR3-Varsche Rivier 003.

Combining both the Conard and Parkington field work, the archaeological deposits have been excavated over an area of 18 m², with a volume of 1.4 m³ and exposed a maximal thickness of 1.5 m. Previous results on the stone artefacts and ochre (Parkington et al., 2004; Will et al., 2013, 2015) as well as shellfish remains (Kyriacou et al., 2015) of both the

147 Parkington and Conard campaigns have already been published. The sequence at HDP1
148 consists of three consecutive archaeological horizons (AH I–III), each containing *in situ* MSA
149 lithic artefacts, ochre, shellfish, terrestrial fauna and abundant fragmented ostrich eggshells
150 (Fig. 2). The strata are in primary context, slope slightly downwards to the south and lie either
151 directly under a thick calcrete carapace or the modern surface (HUMUS). The strata, although
152 intact, have been truncated by erosion in the downslope direction toward the beach. A
153 correlation between excavated units of the Parkington and Conard excavations is possible
154 though not one to one (e.g., AHI consists of facies CESA, SHEM and NOSA in the old
155 excavations). Here we will use both stratigraphic designations to indicate the exact location of
156 the dating samples (Table 1).

157 AH I and III are light-colored strata composed of consolidated fine sand containing many
158 marine shells in both complete and fragmented status. Micromorphological analysis of the
159 deposits (Göden, 2014) show that AH I and III are composed largely (ca 85%) of rounded, sand-
160 sized, calcareous bioclasts with a more minor component of ooids, peloids and glauconite
161 grains. Sand-sized grains of quartz are also present, at around 10-15%. Coarser components
162 include shell fragments and also fragments of calcrete. The bioclastic grains exhibit micritic
163 coatings creating a chitonic c/f-related distribution. Rootlet channels are present in AH I and
164 III (as in all other strata studied at the site) and they exhibit infillings of needle-fibre calcite
165 and well as the local formation of calcite hypocoatings. Anthropogenic components in AH I
166 and III are minor, but consist of fragments of charred organic matter, burnt and unburnt bone,
167 and larger shell fragments. Sandwiched between AH I and III, AH II averages 20 cm and consists
168 of compact, dark brown clay and organic-rich sediments and yielded many, mostly broken,
169 marine shells and abundant quartz artifacts. AH II is readily distinguished from the other two
170 strata based on its darker color, due to the higher content in organic material. It is more
171 heterogeneous than the other units, with both finer grain size and higher content in coarse
172 (>710µm) sedimentary material. Find densities are highest for AH II concerning lithics and
173 faunal remains, yet with all AHs showing comparable densities of shellfish remains (11-13
174 kg/m^3; Will et al., 2015: Table 3). Thin sections analysed from AH II show that this strata, like
175 AH I and III, consists largely of sand-sized, calcareous bioclasts. However, AH II is significantly
176 enriched in finely comminuted organic matter, both carbonized and humified, as well as
177 anthropogenic components such as burnt and unburnt bone, large shell fragments, and

charcoal. The groundmass appears locally phosphatized. Rootlet channels are more numerous in AH II relative to AH I or III and have more pronounced needle-fibre calcite infillings. Below the oldest archaeological horizon, AH III, lies a 2 m thick, sterile, calcareous, shelly sand (SHES) named for its abundant land snails (*Trigonephrus*). SHES rests on top of the paleontological layers of the site. Micromorphological analysis of SHES shows that it is compositionally similar to AH I and III but lacks any significant anthropogenic components.

Nine sediment samples have been taken from the available sections for OSL dating. Samples HDP2, 3 and 7 come from the NOSA/ AHI Unit, HDP1 and 6 from the DAMA/AHII unit, and HDP4 and 8 from the NOSAII/AHIII unit (Table 1 and Fig. 2). HDP5 and 9 were taken at the top of the SHES unit. Within NOSA/AH1, HDP3 is located clearly above HDP2 and 7. The exact stratigraphic relationship between HDP2 and 7, HDP1 and 6, HDP4 and 8, and HDP5 and 9 is not clear and each couple can be considered as a replicate for its stratigraphic unit (Fig. 2). All samples were taken by night under red/orange light, after removing the surface of the sediment previously exposed to sunlight.

OSL sample	elevation (mm)	unit (Parkington)	unit (Conard)
HDP3	5 034	NOSA	AHI
HDP2	4 763		
HDP7	4 593		
HDP1	4 425	DAMA	AHII
HDP6	4 354		
HDP4	4 210	NOSA2	AHIII
HDP8	4 112		
HDP5	4 095	SHES	SHES
HDP9	4 085		

Table 1: Elevation (mm above datum taken with a total station during excavations), and attribution to units (according to both Parkington's and Conard's nomenclature) of the OSL samples.

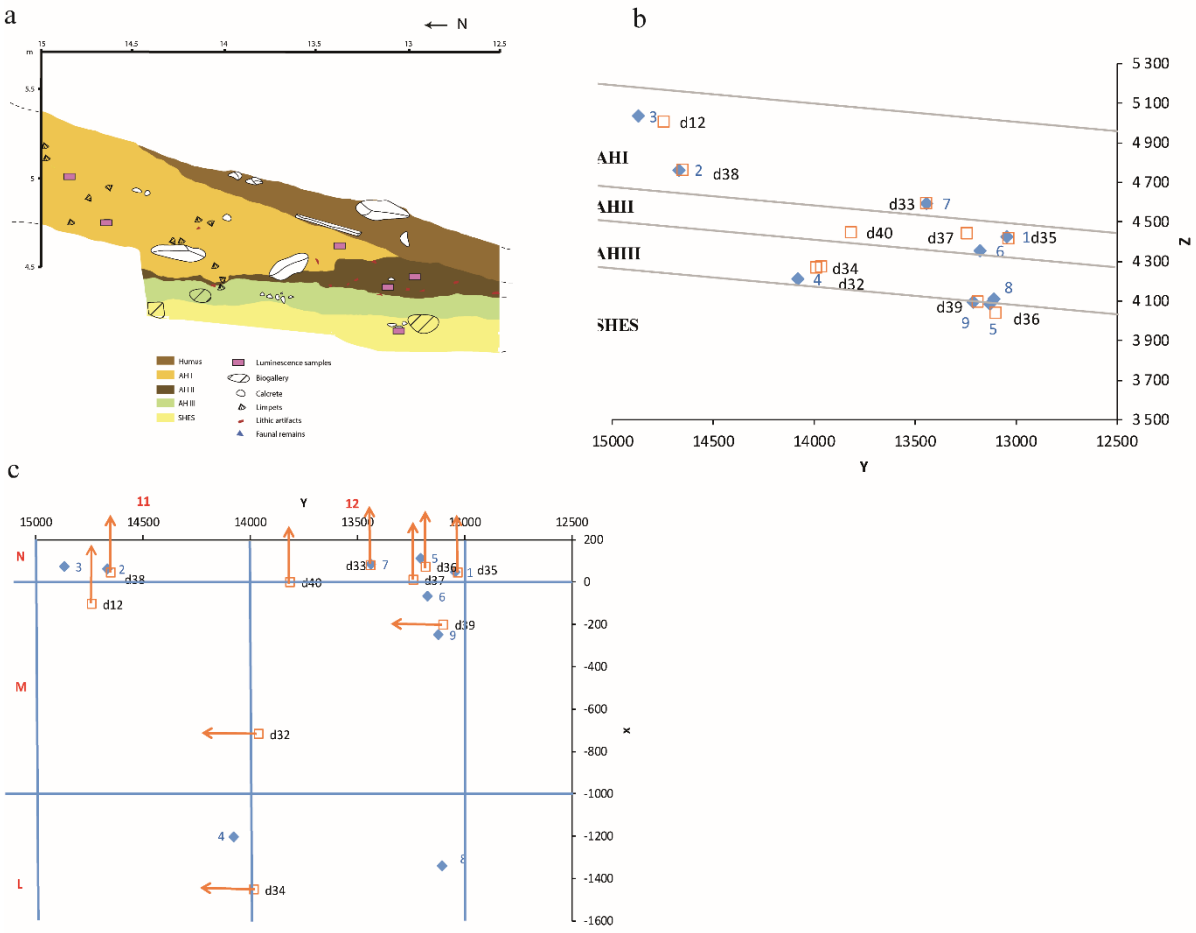

Figure 2: Stratigraphic sketch and location of the sediment samples for OSL dating and dosimeters. a) North-South profile. b) Projection on the profile of the samples (blue diamonds) and dosimeters (red squares); the approximate limits between the units are drawn (grey lines). c) Plan view, with the location of the OSL samples (blue diamonds) and dosimeters; the red squares show the edge of the dosimeter tubes that were apparent while the dosimeters were inserted into the section and were recorded with the total station; the orange arrows symbolise the tube, with the Al_2O3:C chips located at the tip.

3) Equivalent dose determination

3.1 Preparation

The samples have been sieved to 710 µm, dried and weighted. The > 710 µm fraction and part of the < 710 µm were saved for gamma spectrometry analyses (section 4). The rest of the < 710 µm fraction was further treated in order to extract the quartz grains: wet sieving at 100 and 140 µm was followed by HCl (10%), H_2O_2 (30%), heavy liquid separation (heteropolytungstate of sodium at 2.72 and 2.58 g/cm^3). The quartz grains were then HF (40%) etched for 60 min followed by HCl (10%) overnight and a final sieving at 80 µm. Note that feldspar grains were also extracted but their study will not be presented here. The absence of feldspar contamination in the quartz extracts was checked by applying depletion ratio tests,

following Duller (2003).. This was performed mainly on the dose recovery tests and once the sample was claimed clean, this test was not repeated on the De measurements.

The 100-140 µm quartz grains were mounted either on multi-grains discs using silicon oil or on single grain discs displaying 100 holes, each 150 µm diameter and 150 µm deep, so that there was only one grain per hole.

3.2 Measurement devices

Measurements were performed on a Lexsyg Smart for multi-grain measurements and on three Risoe TL/OSL DA 20 single grain devices for single grain measurements (Bøtter-Jensen, 2000, 2003; Richter et al., 2015). Table 2 gathers the main information about the excitation and detection systems that were then used for the Hoedjiespunt samples.

Reader	excitation	detection	source
Lexsyg Smart (multi-grain)	green LED (525 nm)	3mm Schott BG3+ 5 mm Delat BP365/50 EX - interference in front of a H7360-02 PM tube (range 330-380 nm)	90Sr/90Y beta source, 0.19 Gy/s
Risoe TL/DA 20 (single grain)	10 mW Nd:YVO4 diode-pumped green laser (532 nm); IRSL (850nm) LEDs; blue LEDs (525 nm)	7 mmm Hoya U340 in front of Q 9235 PM tube (range: 280-380 nm)	90Sr/90Y beta source, 0.10 to 0.14 Gy/s

Table 2: technical details about the stimulation, detection and irradiation systems of the Risø and Lexsyg luminescence readers used in this work. The 532 nm laser stimulation was used for single grain measurements, the blue LEDs stimulation for multi-grain measurements and the IRSL stimulation for testing the feldspar contamination.

3.3 Protocol

The quartz grains from Hoedjiespunt are dominated by the fast component as shown by a LM-OSL test (Fig. 3). Therefore, a Single Aliquot and Regenerative dose (SAR; Murray and Wintle, 2000, 2003) protocol has been tested and applied (Fig. 4).

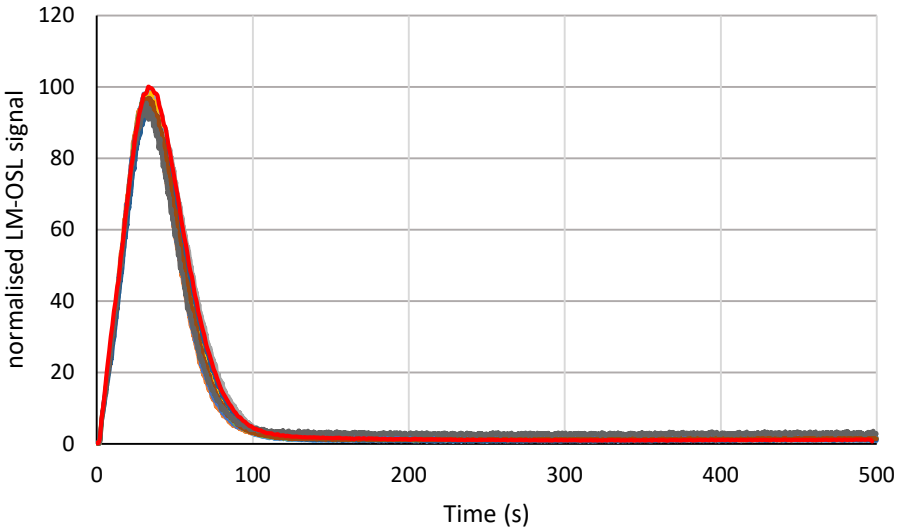

Figure 3: LM-OSL test for all the samples. One multi-grain aliquot of each sample was optically stimulated at 125°C while increasing linearly the stimulation power from 0 to 70 mW/cm^2 in 500 s. The red glow curve corresponds to the calibration quartz from Risø (Hansen et al., 2015), that is known to be dominated by the fast component and is used as a reference.

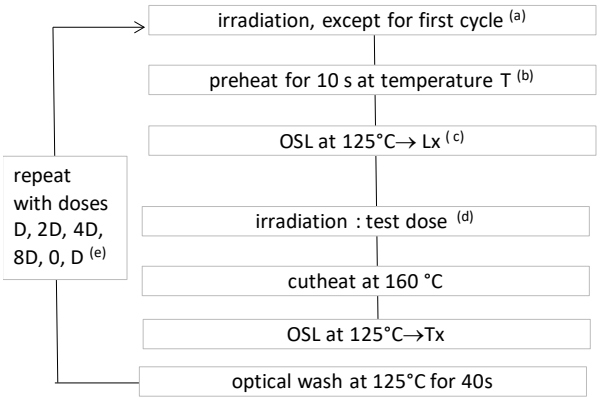

Figure 4: SAR protocol applied for the equivalent dose determination. a) the first cycle corresponds to the measurement of the natural signal; b) T was fixed at 260°C for 10 s; c) the OSL stimulation of single grains was performed for 1.6 s. Lx (and Tx) was calculated from the integration of the first 0.1 s for signal and last 0.20 s for background; d) the test dose was either about 7 Gy or 33 Gy; e) D was about one third of the expected De.

A minimal requirement for SAR is that it allows to recover a known laboratory given dose. A dose recovery test (DRT) was thus performed on single grains aliquots, where the samples were first bleached for one minute in a solar simulator (Honle UVAcube 400), left in the dark at room temperature for at least 10000 s, and bleached again in the reader for 200 s

at 30°C. Then a dose, close to the equivalent dose estimated on multi-grain preliminary runs, was given and the protocol was applied. Analysis of single-grain data was performed with Analyst v4.57 (Duller, 2015). Grains were selected based on the sensitivity of each grain (test dose of the "natural" signal > 3 times background signal; relative error on "natural" test dose signal < 10%), and on the recuperation signal (normalised signal for the zero Gy dose < 5% of the normalised signal of the highest regeneration point). The recycling ratio was not used as a rejection criteria, because one of the luminescence reader is equipped with an heterogeneous radioactive source and corrections are required according to the disc position (CorrSGbin software, provided by DTU Nutech). Apparent irradiation times are re-calculated and thus highlights the grains that have moved significantly between the two recycling cycles and for which the calculation of a recycling ratio is therefore unrelevant. However, considering only the grains for which the recycling ratio could be confidently determined, one found that for these samples there is no correlation between the recycling ratios (most standing between 0.75 and 1.25) and the equivalent doses or overdispersions. This observation is in agreement with Thomsen et al., (2016) and Guérin et al. (2015) who have already argued that, while reasonable, the recycling rejection criteria has no strong impact on the mean/central De calculation (at least on the samples they observed).

The dose response curve was fitted with a saturated exponential such as:

$\frac{Lx}{Tx} = \mathrm{I}_0\left[1 - exp\left(-\frac{(D+b)}{D_0}\right)\right]$, where D is the regenerative dose, Lx/Tx is the normalised luminescence signal and I_0, b and D_0 are fitting parameters. In addition to the grains discarded because of the rejection criteria mentioned above, numerous grains (see Table 3 and 4) were also rejected when no intercept of the normalised natural signal (Ln/Tn) onto the growth curve was possible, i.e., the natural signal is at or above the saturation limit I_0. Beside these usual selection criteria, and following Thomsen et al., (2016), the D_0 value (saturation parameter) was also used as an additional criterion: in practice, the equivalent doses are ranked in function of the corresponding D_0 values and the central doses (after Galbraith et al., 1999) are calculated while progressively discarding the grains with the lowest D_0 values. This leads to increasing central dose values as a function of the D_0 value until a plateau is reached. In addition, the proportion *p* of grains rejected because of the saturation parameter (within the population of grain that pass the first set of rejection criteria) was calculated in function of D_0. The lowest D_0 for accepted grains was thus within the central De plateau, where less than 5%

of grains were rejected because of saturation. Figure 5 displays this analysis for sample HDP3: the final central equivalent dose was calculated for D_0>70 Gy, in the plateau area, where *p*< 5%, in order to avoid any bias due to saturation issues.

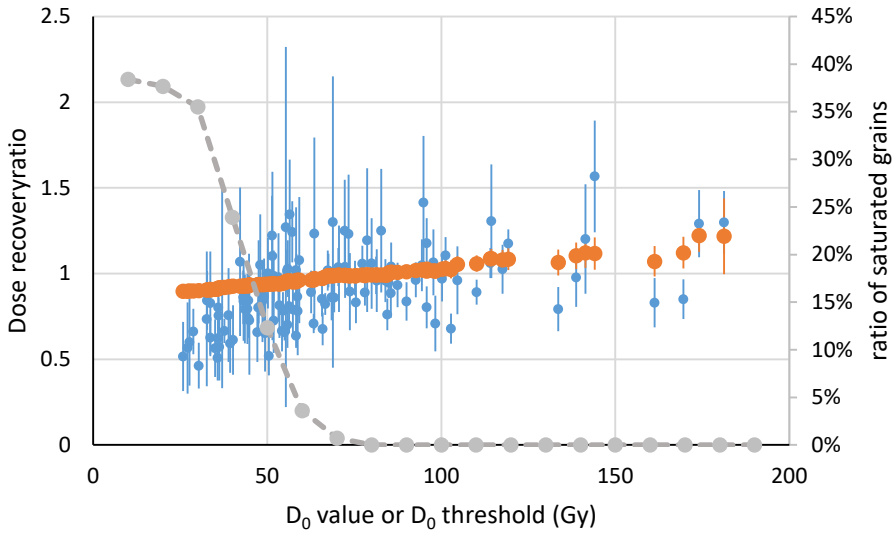

Figure 5: Results of dose recovery tests for HDP3. Blue dots: Dose recovery ratio as a function of D_0 value for each grain that pass the selection criteria and is not saturated. Orange dots: the dose recovery ratio calculated after the CAM in function of the minimum D_0 value considered in the distribution. Note that there are two additional points with much larger D_0 values that have not been plotted here for the clarity of the graphic. Grey dots: percentage of saturated grains over the total number of grains passing the selection criteria, above a D_0 threshold value. The final dose recovery ratio is considered in the plateau region (here above 70 Gy), where less than 5% of the grains show saturation.

sample	tested dose (Gy)	N	n1	n2	n	D_0 (Gy)	dose recovery ratio CAM		OD (%)	
HDP3	100	1000	175	122	38	80	1.00	± 0.03	9	± 3
HDP2	100	1000	69	50	23	80	1.04	± 0.03	7	± 5
HDP7	100	900	195	129	49	80	0.95	± 0.02	8	± 2
HDP1	114	1100	116	67	35	80	0.97	± 0.02	5	± 4
HDP6	159	1000	167	93	12	160	0.97	± 0.03	2	± 11
HDP4	143	900	58	40	16	110	1.00	± 0.05	12	± 5
HDP8	133	500	33	21	11	80	1.02	± 0.05	11	± 5
HDP5	239	1200	154	84	13	200	0.94	± 0.05	8	± 7
HDP9	245	1400	51	23	8	150	0.98	± 0.11	24	± 9

Table 3: Dose recovery ratios. N: number of tested grains. n_1 number of grains passing the selection criteria. n_2: number of grains passing the selection criteria with unsaturated luminescence signals. n: number of grains also passing the D_0 criteria and present in the final De distribution. D_0: threshold value of D_0, above which the (n) final grains are selected. CAM: the calculation of the dose recovery ratio is based on the Central Age Model of Galbraith et al., (1999). OD: overdispersion.

Table 3 shows the results for the dose recovery tests. The relevant "mean" dose is calculated from the Central Age Model (CAM, Galbraith et al., 1999). The ratios of obtained to expected dose are either within 5% of unity and/or consistent with unity at two sigma, and are thus claimed satisfactory. Note that the overdispersion (OD) stands between 2±11 and 24±9 % (mean 10±6 %). Because of the low number of accepted grains, the uncertainty associated to each OD is large, but these values are consistent with 10%-15%, which is not unusual for dose recovery tests (e.g. Thomsen et al., 2016).

3.4 results

The equivalent doses were then measured with the same readers and protocols as for the dose recovery tests. Between 2300 and 8900 grains were analysed for each sample (Table 4). Only 3 to 8% pass the first set of selection criteria and are not saturated. After the D_0 test, 1 to 3% of the measured grains remain in the final De distribution, down to 0.3% for HDP9. It is worth noting that in every De distribution but for HDP1 and 2, a population of grains consistent with a modern age (dose close to 0 Gy) is present (Fig. 6). These low dose grains are not related to a low D_0 value effect. While bioturbations have been observed on these sections (e. g. fine root channels, often associated with rhizolith formation) they do not come with quartz silt infilling. A more likely explanation for the presence of these 0 Gy quartz grains could be the strong wind occurring all the time at that place, which could have polluted the samples during their extraction on the site. The D_0 threshold allows discarding most of these grains however and the grains with negative equivalent dose have been discard before the calculations of the mean/central dose. The few remaining grains have not been discarded, because they are associated with large uncertainties and their weight in the final distribution is negligible, and we wanted to avoid subjective selection. Table 4 displays the equivalent doses, based on the CAM, together with the over-dispersion values. However, the relevance of the CAM here is disputable and further discussed in section 5.

Unit	sample	N	n1	n2	n	$D_{0\,(Gy)}$	Equivalent doses (Gy)											
							CAM		ADM		FMM (CAM based)						logN_M	Gauss
							De	OD (%)	De	OD (%)	1			2				
NOSA/AHI	HDP3	2300	193	146	81	60	77.9 ± 3.5	37 ± 4	82.3 ± 3.5	33 ± 6							81.8 ± 4.4	86.2 ± 4.5
	HDP2	6700	428	288	102	80	88.9 ± 4.5	48 ± 4	98.7 ± 6.2	45 ± 5							90.0 ± 5.7	102.3 ± 6.4
	HDP7	3700	414	314	104	80	84.4 ± 3.8	41 ± 3	90.8 ± 4.1	38 ± 5							80.4 ± 4.6	89.0 ± 4.9
DAMA/AHII	HDP1	4500	377	225	93	90	116.0 ± 4.3	32 ± 3	120.7 ± 4.3	28 ± 3							123.4 ± 4.9	129.3 ± 4.7
	HDP6	7000	580	354	93	120	127.1 ± 6.4	45 ± 4	138.8 ± 7.4	42 ± 5							132.9 ± 8.3	149.1 ± 8.2
NOSA2/AHIII	HDP4	7100	629	373	63	150	150.0 ± 12.5	64 ± 6	181.8 ± 16.8	62 ± 4	91.6 ± 8.6	(54%)	271.0 ± 28.1	(46%)			153.8 ± 13.1	184.1 ± 14.6
	HDP8	7200	716	431	78	120	120.2 ± 7.0	48 ± 4	133.4 ± 9.4	46 ± 5	105.6 ± 10.3	(81%)	217.9 ± 60.0	(19%)			123.4 ± 8.3	139.3 ± 8.4
SHES	HDP5	8900	568	268	61	180	259.3 ± 14.3	40 ± 4	277.9 ± 16.5	37 ± 5							262.8 ± 14.5	279.7 ± 13.5
	HDP9	8200	785	464	24	450	181.1 ± 25.0	65 ± 10	220.8 ± 32.0	63 ± 6	104.4 ± 16.6	(51%)	322.5 ± 53.1	(49%)			275.9 ± 39.2	301.0 ± 36.2

Table 4: Equivalent dose estimates for quartz grains. N, n_1, n_2, n, D_0, CAM, OD: see Table 3. ADM: average dose model, FMM: Finite Mixture Model, LogN_M: Bayesian calculation with a log-normal model and search of the median, Gauss: Bayesian calculation with a Gaussian model

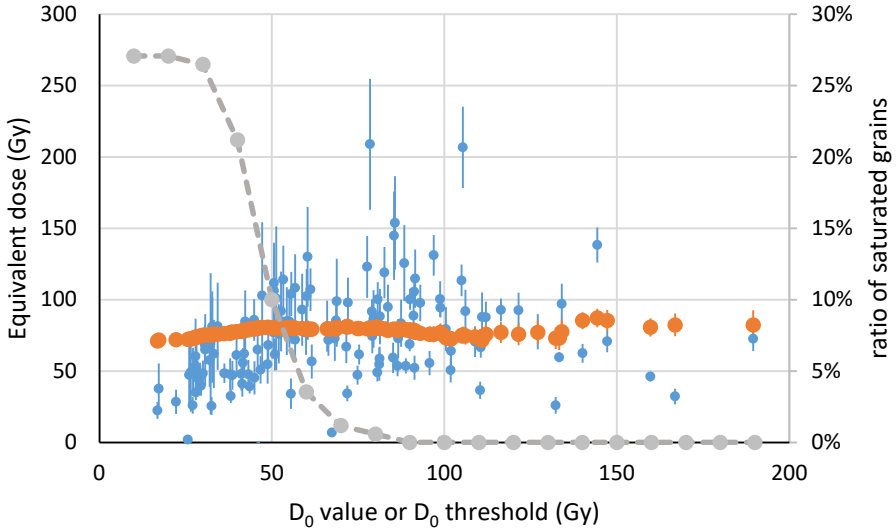

Figure 6: Equivalent dose (De) distribution for sample HDP3. Blue dots: De in function of D_0 value for each grain that pass the selection criteria and is not saturated. Orange dots: De calculated after the CAM in function of the minimum D_0 value considered in the distribution. Note that there are additional points with much larger D_0 values that have not been plotted here for the clarity of the graphic. Grey dots: ratio of the number of saturated grains above a D_0 threshold value, over the total number of grains passing the selection criteria. The final De is considered in the plateau region, where less than 5% of the grains show saturation.

The OD for the equivalent dose measurements stand between 32±3 % and 48±4 % for all samples, but for HDP4 (64±6 %) and HDP9 (65±10 %). Visual inspection of the De distributions for these two samples suggests that they bear two distinct populations (Fig.sup A and C). This is further discussed in section 5.

4) Dose rate

The total dose rate is the sum of the contributions from the gamma, beta and cosmic dose rates. Since the quartz grains have been HF etched, we assume that the alpha dose rate can be neglected.

358 4.1 cosmic and gamma dose rates

359 For the cosmic dose rate, we have applied the equation of Prescott and Hutton, (1994).
360 This takes into account the burial depth of the sample, its geographical coordinates and the
361 thickness and density of the overlaying sediment. We have assumed that the current burial
362 depths were representative of the past mean ones. The cosmic dose rates stand between
363 0.18±0.02 and 0.20±0.02 Gy/ka and represent between 16 to 25% of the total dose rates
364 (Table 5).

365 The gamma dose rates were calculated from *in situ* dosimetry: 10 tubes, each containing
366 3 Al_2O_3:C pellets, have been inserted 30 cm deep into the stratigraphic sections as close as
367 possible from the sediment samples (Fig. 2), and left for about one year (Bøtter-Jensen et al.,
368 1997; Kreutzer et al., 2018). The recorded doses, corrected for the cosmic contribution, show
369 very little scatter (10% RSD on the gamma dose for the 10 tubes, 6% for the total dose over
370 the 30 chips) (Table Sup A), though they are slightly higher for the organic rich DAMA/AHII
371 layer. Each sample was attributed the gamma dose deduced from the closest dosimeter, but
372 for HDP8, for which no close dosimeter was available and thus the mean of all dosimeters was
373 applied.

374 Variation of moisture over time induces variation of the dose rate. The mean past water
375 content should then be taken into account. Meanwhile, it is impossible to precisely assess
376 what it was. Moisture content was measured for the day of sampling (Table 5) and shows high
377 variability among the samples. It seems correlated with the constituents (organic vs shelly):
378 the organic-rich unit (DAMA/AHII) displays water content around 30% (mass of water/mass of
379 dry sediment), while the shelly-sandy units are nearly dry (1% for SHES). In order to at least
380 take these different power of water retention into account, no correction was applied to the
381 gamma dose rates recorded by the dosimeters (since they already take into account the
382 various moisture contents), but a 10% systematic error was arbitrarily added, based on the
383 extreme values that can be calculated if the past and current water content had been
384 drastically different. The gamma doses stand between 0.30±0.04 Gy/ka and 0.41±0.04 Gy/ka.
385 They contribute for 31 to 39% of the total dose rates.

386 4.2 beta dose rates: introduction

387 The beta dose rates for each emitter (K, U, Th) can be calculated following the equation:

388 $$D_{s+w} = \frac{D_s}{1 + k\left(\frac{m_w}{m_s}\right)}$$

389 equivalent to

390

391

392 $$D_{s+w} = \frac{a\delta A_s}{1 + k\left(\frac{m_w}{m_s}\right)}$$

393

394 with, D_{s+w}: beta dose rate for either U or Th or K for the wet sediment; D_s: beta dose rate for either U
395 or Th or K for the dry sediment; m_s: mass of dry sediment; m_w: mass of water; A_s: activity of U or Th, or
396 K content, for the dry sediment; k: correction factor for water content for either U or Th or K; *a*:
397 attenuation factor depending on grain size for either U or Th or K; δ: specific beta dose rate for either
398 U or Th or K.

399 The calculation of the beta dose rates was complicated by the high carbonate content
400 of the sediment (up to 800 % of mass of carbonate over non-carbonated material in the < 710
401 µm fraction; see Table 5 and Table sup A), due to the presence of bioclastic sands, shell and
402 calcrete fragments of all sizes. This raises three distinct questions: 1) Are there significant
403 differences in absorption of radiative energy compare to siliceous materials, i.e. are the
404 attenuation factors *a* and corrections for water contents *k* different from the ones applied in
405 siliceous matrix (Nathan and Mauz, 2008; Guérin et al., 2012)? 2) Is the model of infinite matrix
406 dose rate still applicable (Cunningham, 2016)? 3) What is the impact of this carbonated matrix
407 on the distribution of dose rate, thus on the distribution of equivalent doses and what does it
408 imply for the age (actually dose) model (Mayya et al., 2006; Guérin et al., 2017)? Questions 1
409 and 2 are discussed successively in this section, question 3 will be discussed in section 5.

						dose rates (Gy/ka)													
unit	sample	grain-size	water	% fine/tot	%carbonate	cosmic		gamma		beta1		beta 2		tot1		tot2		mean	
NOSA	HDP3	100-140	7%	69%	558%	0.20	± 0.02	0.31	± 0.03	0.30	± 0.03	0.29	± 0.03	0.82	± 0.05	0.81	± 0.05	0.81	± 0.05
NOSA	HDP2	100-140	10%	70%	676%	0.19	± 0.02	0.35	± 0.04	0.24	± 0.02	0.23	± 0.02	0.78	± 0.05	0.76	± 0.05	0.77	± 0.05
NOSA	HDP7	100-140	17%	50%	473%	0.20	± 0.02	0.34	± 0.04	0.29	± 0.03	0.25	± 0.02	0.83	± 0.05	0.80	± 0.05	0.82	± 0.05
DAMA	HDP1	100-140	28%	25%	152%	0.19	± 0.02	0.41	± 0.04	0.58	± 0.06	0.55	± 0.05	1.18	± 0.08	1.15	± 0.07	1.17	± 0.07
DAMA	HDP6	100-140	22%	42%	97%	0.19	± 0.02	0.39	± 0.04	0.70	± 0.07	0.64	± 0.09	1.29	± 0.08	1.22	± 0.10	1.25	± 0.09
NOSA2	HDP4	100-140	5%	73%	409%	0.18	± 0.02	0.33	± 0.04	0.35	± 0.03	0.35	± 0.03	0.87	± 0.05	0.86	± 0.05	0.86	± 0.05
NOSA2	HDP8	100-140	4%	81%	251%	0.18	± 0.02	0.34	± 0.05	0.39	± 0.03	0.42	± 0.03	0.92	± 0.06	0.94	± 0.06	0.93	± 0.06
SHES	HDP5	100-140	1%	93%	742%	0.18	± 0.02	0.31	± 0.03	0.32	± 0.03			0.81	± 0.05			0.81	± 0.05
SHES	HDP9	100-140	1%	84%	735%	0.18	± 0.02	0.30	± 0.04	0.30	± 0.03			0.78	± 0.05			0.78	± 0.05

410

411 *Table 5: data for dose rates. Water: mass of water over mass of dry sediment. %fine/tot: mass of dry <710µm fraction over*
412 *the total mass of dry sample. %carbonate: mass of carbonate over the mass of dry non- carbonated sediment. Cosmic dose*

rates are deduced from Prescott and Hutton (1994) equation. Gamma dose rates are deduced from field gamma spectrometry. Beta 1 is the beta dose rate calculated from the K, U, Th contents of the <710µm fraction, from high resolution gamma spectrometry, and corrected for water content. Beta 2 is the beta dose rate calculated from the K, U, Th contents of the whole sample, from high resolution gamma spectrometry, and corrected for water content. Tot1 and tot2 are the total dose rates considering beta1 and beta2 respectively. Mean is the average of tot1 and tot2.

4.3 determination of appropriate attenuation factors and water content correction factors.

The attenuation factors *a* and corrections factors *k* in a carbonate-rich matrix were calculated with the DosiVox software (Martin, 2015, Martin et al., 2015a, Martin et al., 2015c), based on the Geant 4 toolkit version 10.01.p01 (Allison et al., 2006, 2016).

The modelled matrix was composed of $Si0_2$ and $CaCO_3$, with a mass ratio ($CaC0_3$ / $Si0_2$) varying from 100% to 800%. The dose received by 120 µm quartz grains was computed in assuming that U, Th and K are uniformly distributed within the carbonate rich matrix. Note that this model differs from the one of Nathan and Mauz (2008), where the carbonate is supposed to fill pores within the sedimentary matrix and be free of any radioactive material. Moreover, these authors only considered $CaCO_3$ contents up to 100% in mass (mass of carbonates over mass of siliceous material).

Attenuation factors *a* deduced from these calculations are shown on Figure 7. They are poorly dependent on the proportion of carbonates. Note, however, that they are significantly different from the ones proposed by Guérin et al., (2012) for a siliceous matrix, but for the potassium (0.96 in both cases): the attenuation factors are here 0.96±0.01 for U, instead of 0.90, and 0.94±0.01 for Th instead of 0.85. These differences are due to the differences of beta absorption between the quartz grains and the matrices and to the method of calculation of the attenuation factor. Guérin et al., (2012) simulated the beta self-doses of SiO_2 grains in a SiO_2 matrix, and calculated the attenuation factors as the complementary of the self-dose. This calculation is possible when the grain and the matrix have the same beta absorption efficiencies. In our case the beta rays coming from the $CaC0_3$ / $Si0_2$ mixed matrix were simulated and the dose was directly evaluated in the SiO_2 grains. Doing this way is important since the quartz self-dose is affected by the mixed matrix because the beta backscattering is different than in a pure $Si0_2$ matrix. Similarly, the attenuation factor is affected because the beta absorption efficiency of a $CaC0_3$ / $Si0_2$ mixed matrix is significantly different from the one of a pure $Si0_2$ matrix.

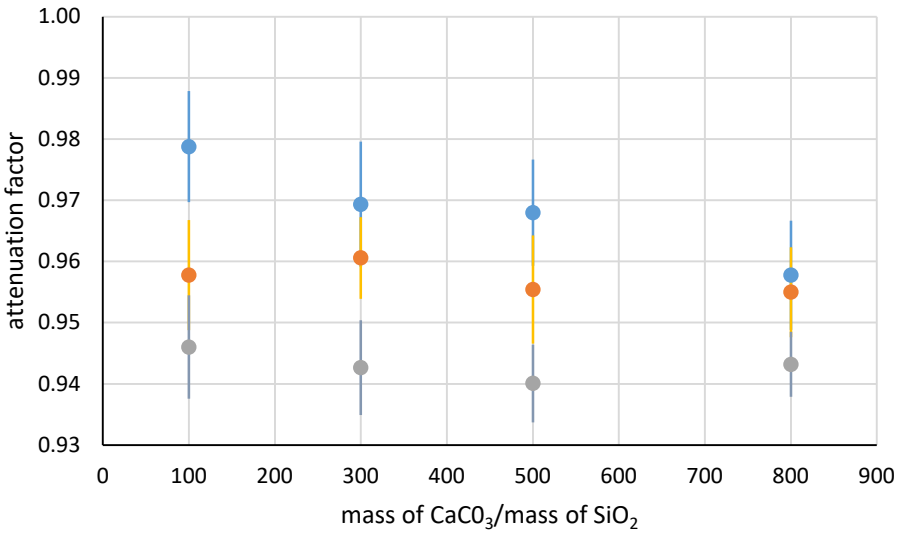

Figure 7: attenuation factors for 120 µm grains, for beta dose from U series (orange dots), Th series (grey dots) and K (blue dots).

Corrections factors *k* for water contents are shown on Fig. 8. Again, they are poorly dependent on the carbonate content. Therefore, means of 1.46±0.04, 1.24±0.04 and 1.14±0.06 were applied respectively for K, U and Th beta dose rates. While they significantly differ from the mean factor of 1.25 calculated by Zimmerman, (1971), but for U, we could observe that the final beta dose rates calculated with both set of correcting factors do not differ by more than 2%. This results from mutual compensations of the difference between the two sets, and so it is likely that significant differences in the calculation of the beta dose rates will only occur in environments where the K, U, Th proportions are significantly different from the standard values. As for the calculation of the gamma dose rates, the current water contents were applied for the calculation of the final beta dose rates.

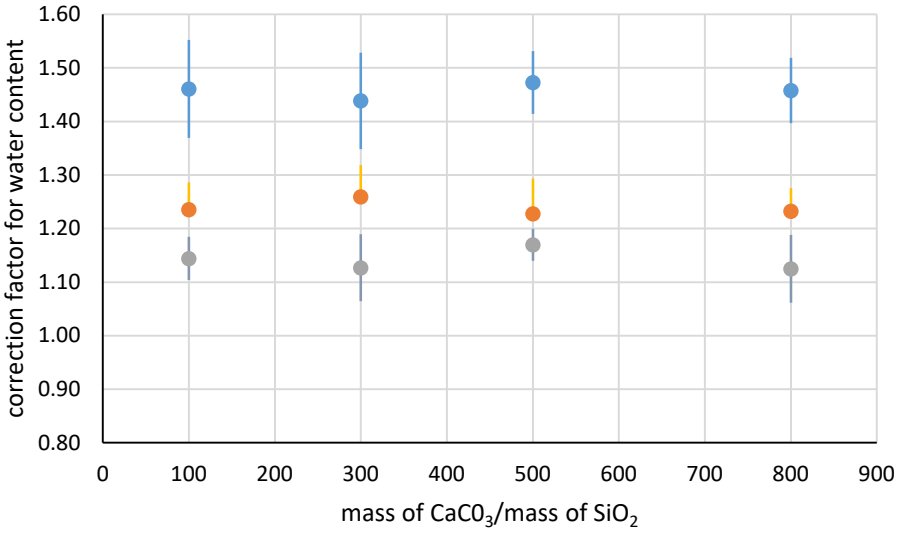

462

463 *Figure 8: correction factor* k for water content *for beta dose from U series (orange dots), Th series (grey dots) and K (blue*
464 *dots).*

465

466 4.4 dealing with heterogeneities.

467

468 Here we deal with the fact that the presence of coarser materials with different matrix
469 and radioactive contents than the fine (here <710µm) fraction where the quartz grains-
470 dosimeters come from, can induce heterogeneities in the beta dose rate (e.g. Martin 2015,
471 Martin et al., 2015b; Tribolo et al., 2017). In particular, Cunningham (2016) warned against
472 the use of the infinite matrix assumption in shell rich sediments, since the shells introduce
473 "cold spots". However we argue here that the heterogeneity of the sediment samples from
474 HDP are not as critical as in the case described by Cunningham. All grain size fractions are rich
475 in carbonates (Table 5 and sup A) and the carbonate contents of the HDP samples are well
476 beyond the ones explored by Cunningham (<40% of total mass in his case). To sum up,
477 whatever the fraction, the matrix is carbonate dominated; this is different from the case
478 where "a few" shells are displayed in a sandy matrix. Moreover, the activities and radioactive
479 contents have limited variations between the <710µm and > 710µm fractions. Those have
480 been determined on a dried, finely crushed (i.e. homogenised) and sealed sub- samples, using
481 high resolution gamma spectrometry (Canberra, e.g. Guibert et al., 2009). Table 6 displays the
482 activities and radioactive contents results.

	Sample HDP	activities (Bq/kg)								content (%)	
		^{238}U series						^{232}Th series		K	
		top		middle		bottom					
fraction < 710µm	3	6.0	± 1.2	11.8	± 0.4	13.5	± 2.1	7.0	± 0.2	0.24	± 0.02
	2	8.2	± 1.1	9.4	± 0.3	5.9	± 2.0	5.4	± 0.2	0.18	± 0.02
	7	8.9	± 0.6	9.6	± 0.2	10.6	± 1.0	6.3	± 0.1	0.27	± 0.01
	1	24.8	± 1.5	15.8	± 0.4	12.7	± 2.4	15.9	± 0.3	0.62	± 0.02
	6	21.9	± 1.2	16.3	± 0.3	12.3	± 1.8	18.6	± 0.3	0.77	± 0.02
	4	10.4	± 1.0	13.4	± 0.3	10.3	± 1.8	6.6	± 0.2	0.26	± 0.01
	8	11.0	± 0.7	14.0	± 0.2	9.5	± 1.2	7.0	± 0.2	0.29	± 0.01
	5	9.2	± 1.0	10.4	± 0.3	8.9	± 1.8	5.3	± 0.2	0.23	± 0.01
	9	8.0	± 0.7	9.5	± 0.2	8.4	± 1.1	4.7	± 0.1	0.23	± 0.01
fraction > 710µm	3	9.6	± 1.1	11.9	± 0.3	8.9	± 1.9	5.9	± 0.2	0.17	± 0.01
	2	10.5	± 1.0	9.3	± 0.3	10.2	± 2.2	4.8	± 0.3	0.12	± 0.02
	7	8.1	± 0.5	7.9	± 0.1	8.4	± 0.9	4.7	± 0.1	0.19	± 0.01
	1	27.4	± 0.9	17.0	± 0.2	13.1	± 1.3	14.4	± 0.2	0.55	± 0.01
	6	21.4	± 0.7	14.5	± 0.2	10.8	± 1.1	14.8	± 0.2	0.62	± 0.01
	4	9.7	± 1.4	14.8	± 0.4	11.1	± 2.2	4.9	± 0.2	0.19	± 0.02
	8	25.0	± 1.4	25.7	± 0.4	12.9	± 2.2	6.4	± 0.2	0.39	± 0.02
	5	nd	nd	nd	nd	nd	nd	nd	nd	nd	nd
	9	nd	nd	nd	nd	nd	nd	nd	nd	nd	nd
total	3	6.9	± 0.9	11.8	± 0.3	12.3	± 1.6	6.7	± 0.2	0.22	± 0.01
	2	9.2	± 0.8	9.3	± 0.2	7.8	± 1.5	5.2	± 0.2	0.15	± 0.01
	7	8.5	± 0.4	8.8	± 0.1	9.5	± 0.7	5.5	± 0.1	0.23	± 0.01
	1	26.7	± 0.8	16.7	± 0.2	13.0	± 1.2	14.8	± 0.2	0.57	± 0.01
	6	21.6	± 0.7	15.3	± 0.2	11.5	± 1.0	16.4	± 0.2	0.68	± 0.01
	4	10.3	± 0.9	13.6	± 0.3	10.4	± 1.6	6.4	± 0.2	0.25	± 0.01
	8	12.7	± 0.7	15.3	± 0.2	9.9	± 1.1	6.9	± 0.1	0.31	± 0.01
	5	9.2	± 1.0	10.4	± 0.3	8.9	± 1.8	5.3	± 0.2	0.23	± 0.01
	9	8.0	± 0.7	9.5	± 0.2	8.4	± 1.1	4.7	± 0.1	0.23	± 0.01

Table 6: activities for ^{238}U series or ^{232}Th series and K contents deduced from high resolution gamma spectrometry. The samples were divided into two distinct fractions: <710µm and >710µm. For the ^{238}U series: the top activities (pre-Rn) are deduced mainly from the ^{234}Th peak, the middle activities (post Rn) are deduced from ^{214}Bi and ^{214} Pb, the bottom activities are related to ^{210}Pb. nd: non determined. The amount of >710µm for HDP5 and HDP9 was assumed negligible (< 16%). The total activities and contents are calculated from the <710µm and >710µm data, weighted by the corresponding mass ratio.

As expected from the nature of each sample and in consistency with the gamma dose rate results, the activities/contents are higher (about 3 times) in the DAMA/AHII organic rich layer than in the shelly layers, for both the <710µm and >710µm fractions. The Th activities and K contents are slightly higher (9±4% to 44±24%) in the <710 µm fraction than in the >710µm fraction (but for K, HDP8), while there is no clear tendency in the U activities, but the differences remain < 25% in most cases. Consequently, there is little difference between the beta dose rate calculated from the < 710µm fraction and the beta dose rate calculated from the entire sample (<2%) (applying the conversion factors δ_i from Guérin et al., 2011). We conclude that the infinite matrix assumption remains a good approximation and the mean

beta dose rate calculated from the fine (<710µm) fraction, and from the entire sample, has been used for the final De calculation.

4.5 beta dose rates: final comments and results

Note (Table 6) that the U series show disequilibrium for most samples: for all but HDP3 and 7, the activity for the middle of the chain (^{226}Ra based on ^{214}Bi and ^{214}Pb) is in excess (13 to 59%) compared to the bottom (based on ^{210}Pb). The middle of the chain is in excess as well compared to the top (based on ^{234}Th) for all samples (up to 29% for most, 97% for HDP3) but for HDP 4 and 8 from NOSA2/AHIII, where a deficit is observed (26 to 36%). The chemical origin of these disequilibria and their local evolution over time is not straightforward and different processes (e.g. radon escape, leaching, etc.) could be involved. However, since U contributes for 20 to 30% of the total dose rate, it can be estimated that in extreme cases where the beta and gamma dose rates are calculated either from the top activities only or from the middle activities only, the total dose rates would not differ by more than 5% for all samples but HDP 3 (12% in this case), compared to a steady case where they are calculated with the current activities. Therefore, the current dose rates (from the current radioisotopic content for the beta dose rate and from the *in situ* dosimetry for the gamma dose rates) were applied to calculate the final age estimates.

The final beta dose rates are, contrary to the gamma dose rates, highly dispersed and stand between 0.23±0.02 Gy/ka and 0.42± 0.03 Gy/ka for the sandy-shelly layers of AHI, AHIII and SHES, and between 0.55±0.04 Gy/ka and 0.70± 0.07 Gy/ka for the organic rich layers of AHII.

5. Ages and discussion

The equivalent dose distributions are widespread, with overdispersions (OD) values standing between 32±3 and 48±4 %, up to 64±6% and 65±10% for HDP4 and HDP9 (Table 4). While a part of this OD might be due to the low presence of modern age grains (thought this is not the case for HDP1 and 2 which have OD similar to those of the other samples), it is likely that a large part of this overdispersion can be attributed to the low K (but also U and Th) contents observed in all the samples: emitters might be far from each other and depending

on the distance between the quartz grains and these emitters, the beta dose rate could be more or less affected (see Mayya et al., 2006; Cunningham et al., 2012; Guérin et al., 2015). These authors have shown on simplified models that, in such a case, the dose rate distribution is positively skewed, and they have questioned the relevance of the central equivalent dose statistical model, such as defined in the Central Age Model (Galbraith, 1999) for calculating the ages (Guérin et al., 2015, 2017; Mayya et al., 2006). They have shown that the Central Age Model calculates the geometric mean of the De distribution, i.e. the median of a lognormal distribution, while the mean dose rate corresponds to an average (arithmetic mean), whatever the Dr distribution. Therefore, in case the Dr and the De distributions are highly skewed, the median and average De will not match and the CAM will lead to age underestimate.

Mayya et al., (2006) and more recently Chauhan et al., (2021) have suggested using a minimum equivalent dose, based on the equivalent dose distribution, together with a minimum dose rate (when the beta K contribution tends to zero; see also, David (2007) and Feathers et al., (2020), for two other similar examples). However, their calculation rests on a simplified model of a quartz matrix sediment with K-feldspar hotspots, in which the size of the K-feldspar grains for a given K content is critical. This information is lacking in the present case, making this model difficult to apply. In addition, it would require a recalculation of the distribution of beta travel range in a carbonated matrix, since it was originally calculated for a siliceous matrix, as well as taking into account the difference in pore space due to the presence of a multiple size fractions in the HDP sediments.

Guérin et al. (2017) have developed another approach where the mean beta dose rate is used (contrary to a minimum beta dose for Mayya et al., 2006), but a weighted average dose is (Average Dose Model) instead of the geometric mean dose of the CAM. Heydari and Guérin (2018) have further tested Bayesian modelling (based on the Baylum R-codes; Philippe et al., 2019). They have shown that the Bayesian approach, associated with Gaussian or Lognormal_median distributions for the prior distribution of the equivalent doses also leads to more accurate results in the case of beta dose rate heterogeneity than the CAM.

De calculated with the different models (CAM, ADM, FMM, Bayesian-Gaussian and Bayesian-logNormal_median) are reported in Table 4. Fig Sup. B helps comparing single component models. For all samples but HDP9, the four De estimates are consistent within 2

562 sigma, though the models based on the calculation of the average (ADM and Bayesian-
563 Gaussian) tend to give higher De than the models based on the calculation of the median (CAM
564 and Bayesian-logNormal_median), as expected for positively skewed distributions.

565 For HDP3, 2, 7, 1 and 6, all models point to ages covering stages 5e to 5c (Fig. 9 and Table
566 7). HDP2 appears to be in chrono-stratigraphic reversal. Compared to HDP7, 1 and 6 below,
567 more grains for this sample have apparent ages over 300 ka (Fig.Sup A), despite a lower mean
568 dose rate. Whether this is due to microdosimetric effects or to another reason is not clear for
569 now.

570 The interpretation for the four lowest samples is more complex. The results for HDP9
571 might be biased due to the low number of selected grains despite the higher number of
572 measured ones. However, the OD of HDP 4 and 9 are higher and the visual inspections of the
573 De distributions (Fig.Sup A and Sup C) suggests that they might be both bi-modal. We applied
574 the FMM (Roberts et al., 2000), with k (number of components) varying between 2 and 4 and
575 sigma_b (OD of each component) varying between 0.2 and 0.4, according to the OD observed
576 for the other samples. In all cases, the BIC and Maximum Likelihood criteria point to two
577 components, with no significant dependence with the value of sigma_b. Results for
578 sigma_b=0.4 have been reported in Table 4. For both HDP4 and HDP9, each component
579 represents ca. 50% of the distribution and the lower components match with the general
580 trend of De close to 100 Gy. The higher components, though imprecise, are both consistent
581 with 300 Gy. HDP4 and HDP9 are close to the stratigraphic junction between SHES and
582 NOSAII/AHIII. The De distributions suggest that there was either a natural (bioturbation)
583 mixing of the two units, or the mixing occurred during the sampling, while the lighting
584 conditions were not optimal to distinguish the stratigraphic limit of the two phases.

585 In theory, it is not reasonable to calculate ages when such mixing occurs (e.g. Tribolo et
586 al., 2010, Guérin et al., 2017) because the significance of the mean dose rate is questionable.
587 However here the total dose rate of the SHES and NOSA2/AHIII samples are close enough to
588 allow this calculation. Consequently, the age for HDP4 would be 106±12 ka, consistent with
589 the marine isotopic stage 5c-5d observed for the upper samples (Table 7). The age for HDP9
590 would be 413±64ka, rather imprecise again due to the low number of selected grains, but not
591 inconsistent with the ages obtained for HDP5 (320±28 to 346±26 ka depending on the statistic
592 model).

unit	sample	Ages (ka)									
		CAM		FMM		ADM		LogN_M		Gauss	
NOSA	HDP3	96	± 8			101	± 8	101	± 8	107	± 8
	HDP2	116	± 10			128	± 12	117	± 10	134	± 11
	HDP7	104	± 9			111	± 9	99	± 8	110	± 9
DAMA	HDP1	99	± 8			104	± 9	106	± 8	111	± 8
	HDP6	102	± 10			111	± 11	107	± 10	120	± 11
NOSA2	HDP4	174	± 19	106	± 12	210	± 24	178	± 18	214	± 20
	HDP8	129	± 12	113	± 11	143	± 15	133	± 12	150	± 13
SHES	HDP5	320	± 28			343	± 31	325	± 25	346	± 26
	HDP9	232	± 36	413	± 64	283	± 46	355	± 54	387	± 53

Table 7: Final ages estimates; CAM: central age model, ADM: average dose model, FMM: finite Mixture Model, LogN_M: Bayesian calculation with a log-normal model and search of the median, Gauss: Bayesian calculation with a Gaussian model. The shaded ages correspond to those that might be less likely, due to possible mixing. Only one component is indicated for the FMM, either corresponding to the main component (HDP8) or the component that seem more consistent with the chronostratigraphic order (HDP4 and 9).

At last, hypotheses can be raised for HDP8. If a single component is considered, i.e. HDP8 was well bleached and unmixed, all models point to ages consistent with the end of MIS6 / start of MIS 5e (129±12 ka to 150±13 ka). But if the same hypothesis of mixing between SHES and NOSAII/AHIII is considered, two components are suggested, the lowest one bearing 80 % of the grains and leading to an age of 113±11 ka, again consistent with the MIS 5c-5e observed for the higher samples, including HDP4.

A Bayesian model including the stratigraphic constraints was tentatively run, but the results (not shown) are not informative and propose an imprecise continuous increase of ages from MIS5c to MIS12.

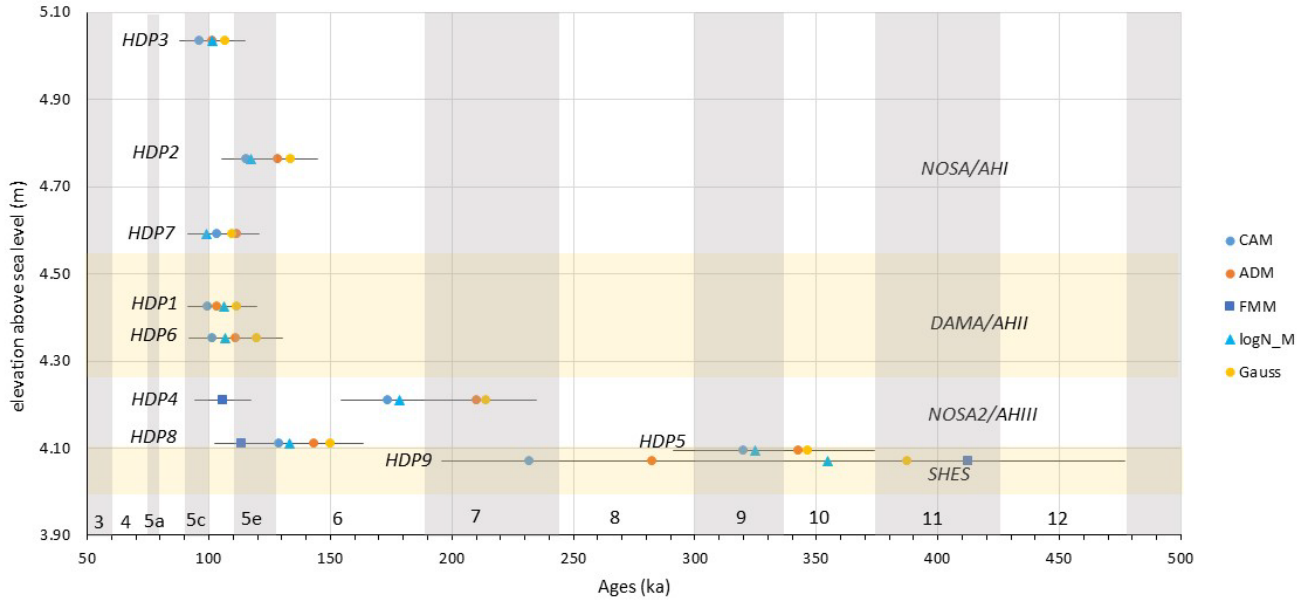

Figure 9: summary of all OSL-quartz ages for different age models. The ages are plotted in function of the elevation. Note however that because the samples do not come from the same stratigraphic column and because of the slope of the deposit the stratigraphic order within a stratigraphic unit is not considered meaningful, but for HDP3 at the top. The Marine Isotopic Stages (MIS) are indicated at the bottom.

In summary, the data suggest that NOSA2/AHIII to NOSA/AHI were most likely deposited during MIS5e-5c. While we could discuss at length the most relevant statistical model, with the "average" based models providing higher estimates than the "median" based models (Guérin et al., 2017, see also Chevrier et al., 2020 for another working example), the general conclusion would remain unchanged due to uncertainties related to water content or burial depth. A mixing, either natural or due to sampling, between NOSA2 and SHES is likely for our samples. SHES is much older than the upper units, likely consistent with MIS9/MIS10. Older ages might also be possible if we consider that the top of SHES remained at the surface, with possible trampling and accidental bleaching for hundreds of years before it was locked by the subsequent units.

The new absolute chronometric ages for HDP1 have further archaeological and evolutionary implications. Combining the older age estimates (Woodborne, 1999, 2000; Parkington, 2003) with our results presented here, we can now firmly place the MSA occupations of HDP1 occurring in the time frame of MIS 5e-c (ca. 130-100 ka) which suggests both a warm climate and a position of HDP1 close to the Atlantic Ocean. These results are consistent with our previous hypotheses (Will et al., 2013, 2015) based on other lines of

evidence. The faunal assemblages feature frequent angulate tortoise as an indicator of warm climates and the abundant remains of shellfish (particularly granite limpets) as well as African penguin and Cape cormorant suggest a close proximity of the site to the sea during deposition of the archaeological layers.

Regional comparisons of lithic artefacts have consistently placed HDP1 within the early part of MIS 5 (e.g., Will et al., 2013; Mackay et al., 2014; Douze et al., 2015; Schmid et al. 2016) and new ages for the similar stone artefact assemblages from Ysterfontein 1 at ~120-113 ka match our results well (Niespolo et al., 2021). Considering the many resemblances in behavioural traces and the close proximity in space and time between Ysterfontein 1 and HDP1, one might speculate on the presence of similar populations or even the same group of early modern humans exploiting the same coastal landscapes in similar ways. Finally, the geographical position of HDP1 at 15-12 meters a.s.l. means that the site would have escaped the maximum MIS 5e sea-level high stand. The convergence of several lines of independent evidence provides a robust age assessment of HDP1 that has been lacking so far.

Importantly, the new ages make HDP1 one of the oldest well-dated open-air sites with good evidence for systematic coastal adaptations. These adaptations encompassed planned and selective gathering of a narrow range of shellfish with a focus on granite limpets and black mussels, anticipated long-distance transport of fine-grained raw materials to the coasts, flexible use of lithic raw materials and the use of ground ochre (Will et al., 2013; Kyriacou et al., 2016), with many similarities to the close-by site of Ysterfontein 1 with comparable antiquity (Avery et al., 2008; Klein et al., 2004; Niespolo et al., 2021). The lithic assemblages at HDP1 are generally small and provide evidence for the import of finished silcrete tools from inland sources at least 10-30 km away. Transport of high-quality raw materials in the form of retouched pieces from inland sources, fragmented reduction chains for silcrete, low find densities and the selected harvesting of small amounts of marine food items indicate a mobility pattern at HDP1 in which well-provisioned individuals executed planned movements to the shoreline with the main aim to exploit shellfish during short-term stays, occurring in a repeated and consistent manner over a 1.5m thick stratigraphic sequence.

Conclusion

Combined with the dating results presented here, we can conclude that early modern humans at HDP1 made consistent use of marine resources and coastal landscapes over many thousand years between ca. 130-100 ka – with several unexcavated localities on the Hoedjiespunt Peninsula occurring in similar stratigraphic positions (e.g., HDP2 and HDP3, see Figure 1) – suggesting successful integration of coastal ecosystems into the regular repertoire of behavioural adaptations by no later than the beginning of the Late Pleistocene. These findings fit recent chronometric dating of sites (Niespolo et al., 2021) and overviews on the increasingly important role of coastal adaptations in the bio-cultural evolution of *Homo sapiens*, with good and persistent evidence for these behaviours over the entire duration of the Late Pleistocene MSA in both southern and northern Africa (Steele and Alvarez-Fernández, 2011; Campmas et al., 2016; Will et al., 2019).

Acknowledgements:

The dating work was initiated under the ANR Emergence ANR-09-JCJC-0123-01 and achieved under the project DAPRES-LA-FEM funded by the Région Nouvelle Aquitaine. Loïc Martin benefits from a Royal Society Newton International Fellowship. The research at HDP1 would not be possible without permission from Heritage Western Cape. Funding for the excavations at HDP1 was provided by the Heidelberg Academy of Sciences and Humanities and the Senckenberg Center for Human Evolution and Palaeoenvironment. We warmly thank John Parkington for introducing us all to this site and want to highlight his important and inspiring contributions on coastal archaeology in South Africa.

Supplementary material:

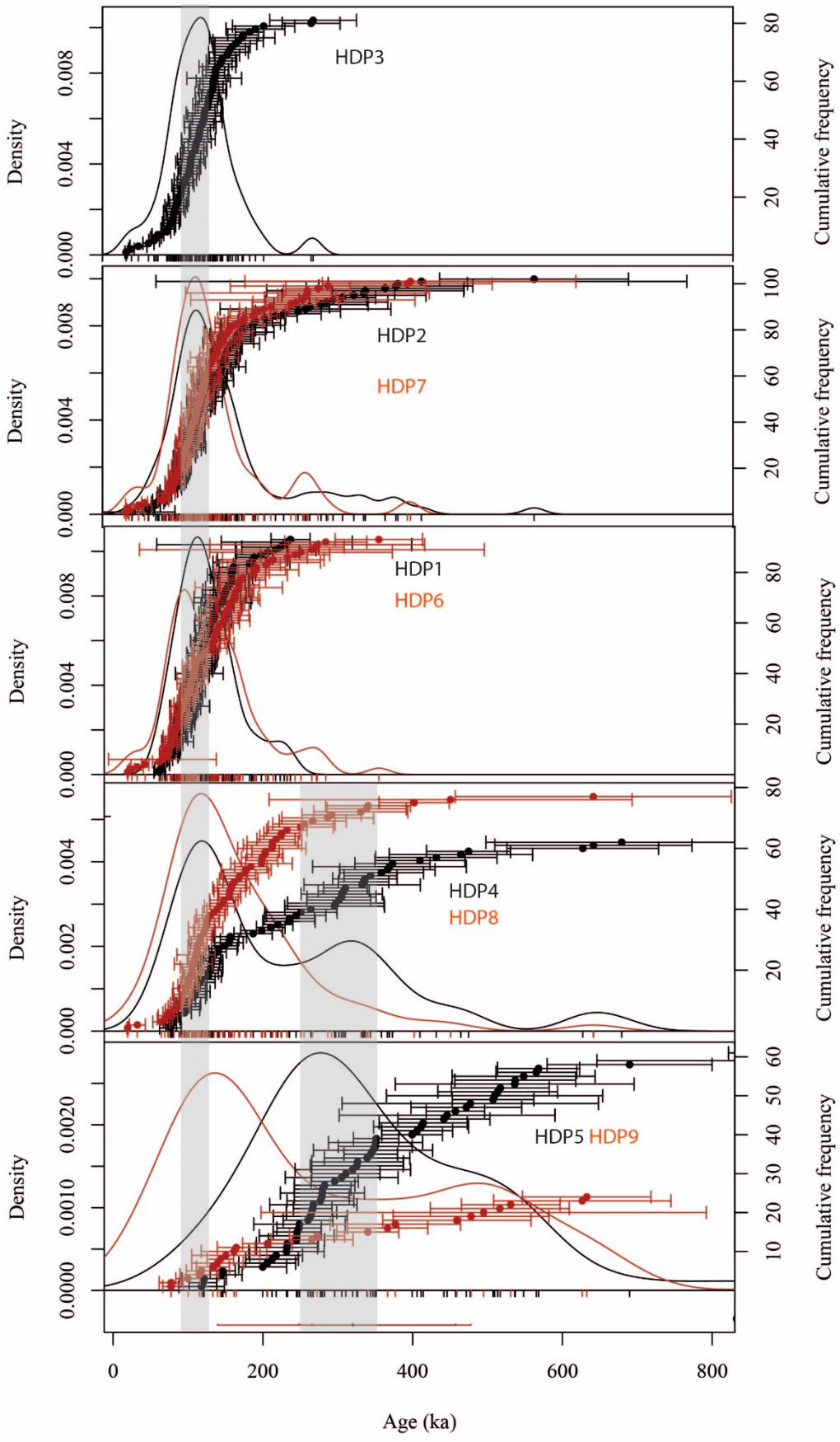
HDP3
HDP2
HDP7
HDP1
HDP6
HDP4
HDP8
HDP5 HDP9
Density
Cumulative frequency
Age (ka)
0
200
400
600
800

688

Figure Sup A (previous page): Ages for individual grains for all samples and Kernel density plots. Note that all the peaks do not necessarily have a meaning. The plots are in the stratigraphic order. The grey bars highlight the periods around 110 and 300 ka, corresponding to the two main peaks.

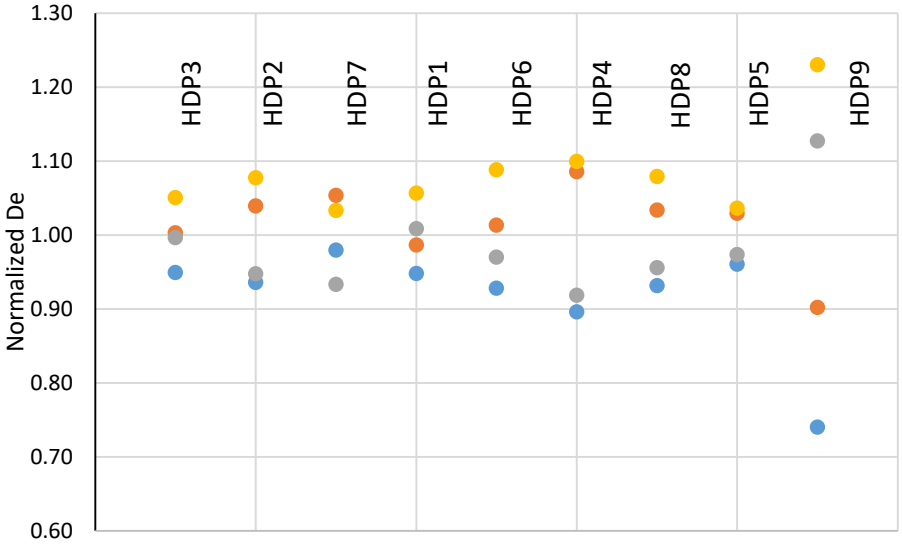

Figure Sup B : comparison of the different De estimates, normalized to the mean De for each sample. Blue dots: CAM; Grey dots: Bayesian-Gaussian; orange dots: ADM; yellow dots: Bayesian-Gaussian. Error bars are not plotted for sake of clarity.

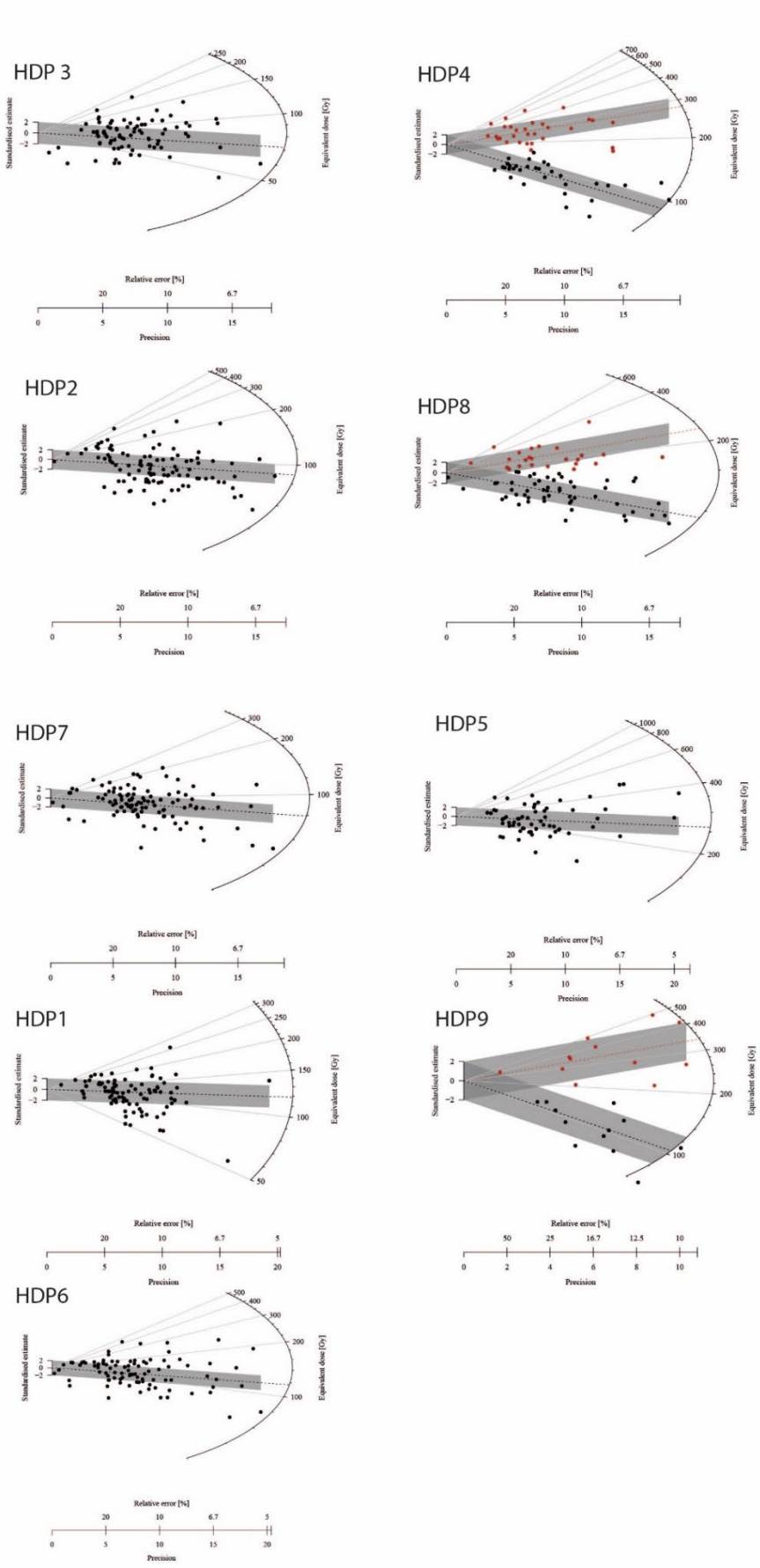

Fig Sup C: radial plots for each sample (based on the selected grains). The colored bands corresponds to either the CAM De or to the components of the FMM.

a	mass of carbonate/mass of siliceous material							
sample	> 1cm		1cm - 2mm		2mm - 710 µm		<710 µm	
HDP3	1950%	±456%	748%	±51%	755%	±54%	558%	±8%
HDP2	620%	±178%	889%	±66%	914%	±93%	612%	±9%
HDP7	1367%	±321%	340%	±7%	863%	±45%	473%	±6%
HDP1	101%	±3%	86%	±2%	82%	±2%	152%	±3%
HDP6	150%	±3%	nd	nd	139%	±3%	97%	±1%
HDP4	1209%	±155%	668%	±34%	619%	±42%	409%	±4%
HDP8	308%	±5%	825%	±37%	640%	±46%	421%	±1%
HDP5	860%	±122%	1100%	±518%	750%	±267%	742%	±7%
HDP9	742%	±34%	767%	±40%	771%	±35%	735%	±3%

b	mass of carbonate/mass of siliceous+carbonated material							
sample	> 1cm		1cm - 2mm		2mm - 710 µm		<710 µm	
HDP3	95%	±22%	88%	±6%	88%	±6%	85%	1%
HDP2	86%	±25%	90%	±7%	90%	±9%	86%	1%
HDP7	93%	±22%	77%	±2%	90%	±5%	83%	1%
HDP1	50%	±1%	46%	±1%	45%	±1%	60%	1%
HDP6	60%	±1%	nd	nd	58%	±1%	49%	1%
HDP4	92%	±12%	87%	±4%	86%	±6%	80%	1%
HDP8	76%	±1%	89%	±4%	86%	±6%	81%	0%
HDP5	90%	±13%	92%	±43%	88%	±31%	88%	1%
HDP9	88%	±4%	88%	±5%	89%	±4%	88%	0%

Table Sup A : carbonate contents for the different fractions a) expressed as mass of carbonate over mass of non-carbonated material b) expressed as mass of carbonate over total mass of sediment.

References

Allison, J., Amako, K., Apostolakis, J., Araujo, H., Dubois, P.A., Asai, M., Barrand, G., Capra, R., Chauvie, S., Chytracek, R., Cirrone, G.A.P., Cooperman, G., Cosmo, G., Cuttone, G., Daquino, G.G., Donszelmann, M., Dressel, M., Folger, G., Foppiano, F., Generowicz, J., Grichine, V., Guatelli, S., Gumplinger, P., Heikkinen, A., Hrivnacova, I., Howard, A., Incerti, S., Ivanchenko, V., Johnson, T., Jones, F., Koi, T., Kokoulin, R., Kossov, M., Kurashige, H., Lara, V., Larsson, S., Lei, F., Link, O., Longo, F., Maire, M., Mantero, A., Mascialino, B., McLaren, I., Lorenzo, P.M., Minamimoto, K., Murakami, K., Nieminen, P., Pandola, L., Parlati, S., Peralta, L., Perl, J., Pfeiffer, A., Pia, M.G., Ribon, A., Rodrigues, P., Russo, G., Sadilov, S., Santin, G., Sasaki, T., Smith, D., Starkov, N., Tanaka, S., Tcherniaev, E., Tome, B., Trindade, A., Truscott, P., Urban, L., Verderi, M., Walkden, A., Wellisch, J.P., Williams, D.C., Wright, D., Yoshida, H., 2006. Geant4 developments and applications. Nuclear Science, IEEE Transactions on. 53(1), 270-278.

Allison, J., Amako, K., Apostolakis, J., Arce, P., Asai, M., Aso, T., Bagli, E., Bagulya, A., Banerjee, S., Barrand, G., Beck, B.R., Bogdanov, A.G., Brandt, D., Brown, J.M.C., Burkhardt, H., Canal, Ph., Cano-Ott, D., Chauvie, S., Cho, K., Cirrone, G.A.P., Cooperman, G., Cortés-Giraldo, M.A., Cosmo, G., Cuttone, G., Depaola, G., Desorgher, L., Dong, X., Dotti, A.,

725 Elvira, V.D., Folger, G., Francis, Z., Galoyan, A., Garnier, L., Gayer, M., Genser, K.L.,
726 Grichine, V.M., Guatelli, S., Guèye, P., Gumplinger, P., Howard, A.S., Hřivnáčová, I.,
727 Hwang, S., Incerti, S., Ivanchenko, A., Ivanchenko, V.N. , Jones, F.W., Jun, S.Y.,
728 Kaitaniemi, P., Karakatsanis, N., Karamitros, M., Kelsey, M., Kimura, A., Koi, T.,
729 Kurashige, H., Lechner, A., Lee, S.B., Longo, F., Maire, M., Mancusi, D., Mantero, A.,
730 Mendoza, E., Morgan, B., Murakami, K., Nikitina, T., Pandola, L., Paprocki, P., Perl, J.,
731 Petrović, I., Pia, M.G., Pokorski, W., Quesada, J.M., Raine, M., Reis, M.A., Ribon, A.,
732 Ristić Fira, A., Romano, F., Russo, G., Santin, G., Sasaki, T., Sawkey, D., Shin, J.I.,
733 Strakovsky, I.I., Taborda, A., Tanaka, S., Tomé, B., Toshito, T., Tran, H.N., Truscott, P.R.,
734 Urban, L., Uzhinsky, V., Verbeke, J.M., Verderi, M., Wendt, B.L., Wenzel, H., Wright,
735 D.H., Wright, D.M., Yamashita, T., Yarba, J., Yoshida, H., 2016. Recent developments in
736 GEANT4. Nuclear Instruments and Methods in Physics Research. A 835, 186–225.
737 Avery, G., Halkett, D., Orton, J., Steele, T., Tusenius, M., Klein, R., 2008. The Ysterfontein 1
738 Middle Stone Age rock shelter and the evolution of coastal foraging. Goodwin Series. 10,
739 66–89.
740 Berger, L.R., Parkington J.E., 1995. Brief communication: A new Pleistocene hominid-bearing
741 locality at Hoedjiespunt, South Africa. Am. J. Phys. Anthropol. 98, 601–609.
742 Bøtter-Jensen, L., Agersnap Larsen, N., Markey, B.G., McKeever, S.W.S., 1997. Al2O3:C as a
743 sensitive OSL dosimeter for rapid assessment of environmental photon dose rates.
744 Radiation Measurements. 27,2, 295-298.
745 Bøtter-Jensen, L., Bulur, E., Duller, G.A.T., Murray, A.S., 2000. Advances in luminescence
746 instrument systems. Radiation Measurements. 32, 523–528.
747 Bøtter-Jensen, L., Andersen, C.E., Duller, G.A.T., Murray, A.S. 2003. Developments in radiation,
748 stimulation and observation facilities in luminescence measurements. Radiation
749 Measurements. 37, 535–541.
750 Brink, J.S., Deacon H.J., 1982. A study of a last interglacial shell midden and bone accumulation
751 at Herolds Bay, Cape Province, South Africa. Palaeoecology of Africa. 15, 31–40.
752 Broadhurst, C.L., Wang, Y., Crawford, M.A., Cunnane, S.C., Parkington, J.E., Schmidt, W. F., 2002.
753 Brain-specific lipids from marine, lacustrine, or terrestrial food resources: potential
754 impact on early African Homo sapiens. Comparative Biochemistry and Physiology B. 131,
755 653–673.
756 Butzer, K.W., 2004. Coastal eolian sands, paleosols, and Pleistocene geoarchaeology of the
757 Southwestern Cape, South Africa. J. Archaeol. Sci. 31, 1743–1781.
758 Campmas, E., Amani, F., Morala, A., Debénath, A., El Hajraoui, M.A., Nespoulet, R., 2016. Initial
759 insights into Aterian hunter–gatherer settlements on coastal landscapes: the example of
760 Unit 8 of El Mnasra Cave (Témara, Morocco). Quaternary International. 413, 5-20.
761 Carr, A. S., Bateman, M. D., Roberts, D. L., Murray-Wallace, C. V., Jacobs, Z., & Holmes, P. J.
762 (2010). The last interglacial sea-level high stand on the southern Cape coastline of South
763 Africa. Quaternary Research, 73(2), 351-363.
764 Chauhan, N., Selvam, T. P., Anand, S., Shinde, D. P., Mayya, Y. S., Feathers, J. K., Singhvi, A. K.
765 (2021). Distribution of natural beta dose to individual grains in sediments. Proceedings
766 of the Indian National Science Academy, 1-15.
767 Chevrier, B., Lespez, L., Lebrun, B., Garnier, A., Tribolo, C., Rasse, M., Guérin, G., Mercier, N.,
768 Camara, A., Ndiaye, M., Huysecom, E., 2020. New data on settlement and environment

769 at the Pleistocene/Holocene boundary in Sudano-Sahelian West Africa: Interdisciplinary
770 investigation at Fatandi V, Eastern Senegal. PLoS One. 15(12), e0243129.
771 Churchill, S. E., Berger, L.R., Parkington, J.E., 2000. A Middle Pleistocene human tibia from
772 Hoedjiespunt, Western Cape, South Africa. S. Afr. J. Sci. 96, 367–368.
773 Cortés-Sánchez, M., Morales-Muniz, A., Simón-Vallejo, M.D., Lozano-Francisco, M.,Vera-Peláez,
774 J.L., Finlayson, C., Rodríguez-Vidal, J., Delgado-Huertas, A., Jiménez-Espejo, F.J., Martínez-
775 Ruiz, F., Martinez-Aguirre, M.A., Pascual-Granged, A.J.,Bergadà-Zapata, M., Gibaja-Bao,
776 J.F., Riqueime-Cantal, J.A., López-Sáez, J.A.,Rodrigo-Gámiz, M., Sakai, S., Sugisaki, S.,
777 Finlayson, G., Fa, D.A., Bicho, N.F., 2011. Earliest known use of marine resources by
778 Neanderthals. PLoS One. 6, e24026.
779 Cunnane, S.C., Stewart, K.M., 2010. Human brain evolution – The influence of freshwater and
780 marine food resources. New Jersey: Wiley-Blackwell.
781 Cunningham, A.C., 2016. External beta dose rates to mineral grains in shell-rich sediment.
782 Ancient TL, 34, 1-5.
783 Crawford, M.A., Bloom, M., Broadhurst, C.L., Schmidt, W.F., Cunnane, S.C., Galli, C.,
784 Gehbremeskel, K., Linseisen, F., Lloyd-Smith, J., Parkington, J.E., 1999. Evidence for the
785 unique function of docosahexaenoic acid during the evolution of the modern hominid
786 brain. Lipids. 34, 39–47.
787 David, B., Roberts, R. G., Magee, J., Mialanes, J., Turney, C., Bird, M., White, C., Fifield, L.K.,
788 Tibby, J., 2007. Sediment mixing at Nonda Rock: investigations of stratigraphic integrity
789 at an early archaeological site in northern Australia and implications for the human
790 colonisation of the continent. Journal of Quaternary Science: Published for the
791 Quaternary Research Association. 22(5), 449-479.
792 Dibble, H.L., Aldeias, V., Alvarez-Fernandez, E., Blackwell, B.A.B., Hallett-Desguez, E.,Jacobs, Z.,
793 Goldberg, P., Lin, S.C., Morala, A., Meyer, M.C., Olszewski, D.I., Reed, K.,Reed, D., Rezek,
794 Z., Richter, D., Roberts, R.G., Sandgathe, D., Schurmans, U.,Skinner, A.R., Steele, T.E., El-
795 Hajraoui, M., 2012. New excavations at the site of Contrebandiers cave, Morocco.
796 PaleoAnthropology. 2012, 145-201.
797 Douze, K., Wurz, S., & Henshilwood, C. S. (2015). Techno-cultural characterization of the MIS
798 5 (c. 105–90 Ka) lithic industries at Blombos Cave, Southern Cape, South Africa. PloS one,
799 10(11), e0142151.
800 Duller, G.A.T., 2003. Distinguishing quartz and feldspar in single grain luminescence
801 measurements. Radiation Measurements. 37, 161–165.
802 Duller, G.A.T., 2015. The Analyst software package for luminescence data: overview and
803 recent improvements. Ancient TL. 33, 35–42.
804 Erlandson, J.M., 2001. The archaeology of aquatic adaptations: paradigms for a new
805 millennium. Journal of Archaeological Research. 9, 287–350.
806 Faulkner, P., Miller, J. M., Quintana Morales, E. M., Crowther, A., Shipton, C., Ndiema, E., ... &
807 Petraglia, M. D. (2021). 67,000 years of coastal engagement at Panga ya Saidi, eastern
808 Africa. Plos one, 16(8), e0256761.
809 Feathers, J. K., Evans, M., Stratford, D. J., de la Peña, P., 2020. Exploring complexity in
810 luminescence dating of quartz and feldspars at the Middle Stone Age site of Mwulu's
811 cave (Limpopo, South Africa). Quaternary Geochronology. 59, 101092.

Galbraith, R.F., Roberts, R.G., Laslett, G.M., Yoshida, H., Olley, J.M., 1999. Optical dating of single and multiple grains of quartz from Jinmium rock shelter, northern Australia: Part I, experimental design and statistical models. Archaeometry. 41(2), 339-364.

Grine, F.E., Klein, R.G., Volman, T.P., 1991. Dating, archaeology and human fossils from the Middle Stone Age levels of Die Kelders, South Africa. Journal of Human Evolution. 21, 363–395.

Göden, M., 2014. Geoarchäologische Untersuchungen zur Fundplatzgenese von Hoedjiespunt 1, Western Cape, Südafrika. Unpublished Masters Thesis, University of Tübingen.

Guérin, G., Mercier, N., Adamiec, G., 2011. Dose rate conversion factors: update. Ancient TL. 29, 5–8.

Guérin, G., Mercier, N., Nathan, R., Adamiec, G., Lefrais, Y., 2012. On the use of the infinite matrix assumption and associated concepts: A critical review. Radiation Measurements. 47, 778–85.

Guérin, G., Frouin, M., Talamo, S., Aldeias, V., Bruxelles, L., Chiotti, L., Dibble, H.L., Goldberg, P., Hublin, J.-J., Jain, M., Lahaye, C., Madelaine, S., Maureille, B., McPherron, S.J.P., Mercier, N., Murray, A.S., Sandgathe, D., Steele, T.E., Thomsen, K.J., Turq, A., 2015. A multi-method luminescence dating of the Palaeolithic sequence of La Ferrassie based on new excavations adjacent to the La Ferrassie 1 and 2 skeletons. Journal of Archaeological Science. 58, 147-166.

Guérin, G., Christophe, C., Philippe, A., Murray, A.S., Thomsen, K.J., Tribolo, C., Urbanova, P., Jain, M., Guibert, P., Mercier, N., Kreutzer, S., Lahaye, C., 2017. Absorbed dose, equivalent dose, measured dose rates, and implications for OSL age estimates: 1 introducing the Average Dose Model. Quaternary Geochronology. 41, 163-173

Guibert, P., Lahaye, C., Bechtel, F., 2009. The importance of U-series disequilibrium of sediments in luminescence dating: a case study at the Roc de Marsal cave (Dordogne, France). Radiation Measurements. 44(3), 223-231.

Hansen, V., Murray, A., Buylaert, J.P., Yeo, E.Y.,Thomsen, K., 2015. A new irradiated quartz for beta source calibration. Radiation Measurements. 81, 123-127.

Hearty, P.J., Hollin, J.T., Neumann, A.C., O'Leary, M.J., McCulloch, M.T., 2007. Global sea-level fluctuations during the Last Interglaciation (MIS 5e). Quatern. Sci. Rev. 26, 2090-2112.

Henshilwood, C.S., Sealy, J., Yates, R., Cruz-Uribe, K., Goldberg, P., Grine, F.E., Klein, R.G., Poggenpoel, C., van Niekerk, K., Watts, I., 2001. Blombos Cave, Southern Cape, South Africa: preliminary report on the 1992–1999 excavations of the Middle Stone Age levels. Journal of Archaeological Science. 28, 421–448.

Henshilwood, C.S., van Niekerk, K.L., Wurz, S., Delagnes, A., Armitage, S.J.,Rifkin, R.F., Douze, K., Keene, P., Haaland, M.M., Reynard, J., Discamps, E., Mienies, S.S., 2014. Klipdrift Shelter, Southern Cape, South Africa: preliminary report on the Howiesons Poort layers. Journal of Archaeological Science. 45, 284–303.

Heydari, M., Guérin, G., 2018. OSL signal saturation and dose rate variability: Investigating the behaviour of different statistical models. Radiation Measurements. 120, 96-103.

Inskeep, R.R., Avery, G., Klein, R.G., Morris, A.G., Poggenpoel, C.A., Vogel, J.C., 1987. Nelson Bay Cave, Cape Province, South Africa: the Holocene levels. International Series 357, BAR.

Jerardino, A., Marean, C.W., 2010. Shellfish gathering, marine palaeoecology and modern human behavior: perspectives from Cave PP13B, Pinnacle Point, South Africa. Journal of Human Evolution. 59, 412-424.

Klein, R.G., Avery, G., Cruz-Uribe, K., Halkett, D.J., Parkington, J.E., Steele, T., Volman, T.P., Yates, R.J., 2004. The Ysterfontein 1 Middle Stone Age site, South Africa, and early human exploitation of coastal resources. Proceedings of the National Academy of Sciences USA 101, 5708–5715.

Klein, R.G., Steele, T.E., 2008. Gibraltar data are too sparse to inform on Neanderthal exploitation of coastal resources. Proceedings of the National Academy of Sciences USA. 105, 20047.

Kreutzer, S., Martin, L., Guérin, G., Tribolo, C., Selva, P., Mercier, N., 2018.Environmental dose rate determination using a passive dosimeter: techniques and workflow for alpha-Al2O3:Chips. Geochronometria, 45, 56–67.

Kyriacou, K., Parkington, J.E., Marais, A.D., Braun, D.R., 2014. Nutrition, modernity and the archaeological record: coastal resources and nutrition among Middle Stone Age hunter-gatherers on the Western Cape coast of South Africa. Journal of Human Evolution. 77, 64–73.

Kyriacou, K., Parkington, J.E., Will, M., Braun, D.R., 2015. Middle and Later Stone Age shellfish exploitation strategies and coastal foraging at Hoedjiespunt and Lynch Point, Saldanha Bay, South Africa. Journal of Archaeological Science, 57, 197–206.

Langejans, G.H.J., van Niekerk, K.L., Dusseldorp, G.L., Thackeray, J.F., 2012. Middle Stone Age shellfish exploitation: Potential indications for mass collecting and resource intensification at Blombos Cave and Klasies River, South Africa. Quaternary International. 280, 80–94.

Mackay, A., Stewart, B.A. & Chase, B.M. 2014. Coalescence and fragmentation in the late Pleistocene archaeology of southernmost Africa. Journal of Human Evolution 72: 1–26.

Marean, C.W., 2011. Coastal South Africa and the co-evolution of the modern human lineage and the coastal adaptation, in Bicho,N., Haws, J.A., Davis, L.G. (Eds.), Trekking the shore: changing coastlines and the antiquity of coastal settlement. New York, Springer, pp. 421-440.

Marean, C.W., 2014. The origins and significance of coastal resource use in Africa and Western Eurasia. Journal of Human Evolution. 77, 17–40.

Marean, C.W., 2016. The transition to foraging for dense and predictable resources and its impact on the evolution of modern humans. Philosophical Transactions of the Royal Society B. 371, 20150239.

Marean, C.W., Goldberg, P., Avery, G., Grine, F.E., Klein, R.G., 2000. Middle Stone Age stratigraphy and excavations at Die Kelders Cave 1 (Western Cape Province, South Africa): the 1992, 1993, and 1995 field seasons. Journal of Human Evolution. 38, 7-42

Marean, C.W., Bar-Matthews, M., Bernatchez, J., Fisher, E., Goldberg, P., Herries, A.I.,Jacobs, Z., Jerardino, A., Karkanas, P., Minichillo, T., Nilssen, P.J., Thompson, E.,Watts, I., Williams, H (2007). Early human use of marine resources and pigment in South Africa during the Middle Pleistocene. Nature, 449, 905-908.

Martin, L., 2015. Caractérisation et modélisation d'objets archéologiques en vue de leur datation par des méthodes paléo-dosimétriques. Simulation des paramètres dosimétriques sous Geant4. PhD thesis, University of Bordeaux Montaigne.

900 Martin, L., Incerti, S., Mercier, N., 2015a. DosiVox: a Geant 4-based software for dosimetry
901 simulations relevant to luminescence and ESR dating techniques. Ancient TL. 33, 1, 1-10.
902 Martin, L., Mercier, N., Incerti, S., Lefrais, Y., Pecheyran, C., Guerin, G., Jarry, M., Bruxelles, L.,
903 Bon, F., Pallier C., 2015b. Dosimetric study of sediments at the Beta dose rate scale:
904 characterization and modelization with the DosiVox software. Radiation Measurements
905 81, 134-141
906 Martin, L., Incerti, S., Mercier, N., 2015c. Comparison of DosiVox simulation results with
907 tabulated data and standard calculations. Ancient TL. 33, 2, 1-9
908 Mayya, Y.S., Morthekai, P., Murari, M.K., Singhvi, A.K., 2006. Towards quantifying beta
909 microdosimetric effects in single-grain quartz dose distribution. Radiation
910 Measurements. 41, 1032-1039.
911 Mellars, P., Gori, K.C., Carr, M., Soares, P.A., Richards, M. B., 2013. Genetic and archaeological
912 perspectives on the initial modern human colonization of southern Asia. Proceedings of
913 the National Academy of Sciences USA. 110, 10699–10700.
914 Miller, K.G., Kominz, M.A., Browning, J.V., Wright, J.D., Mountain, G.S., Katz, M.E., Sugarman,
915 P.J., Cramer, B.S., Christie-Blick, N., Pekar, S.F., 2005. The Phanerozoic record of global
916 sea-level change. Science 310, 1293-1298.
917 Murray, A.S., Wintle, A.G., 2000. Luminescence dating of quartz using an improved single-
918 aliquot regenerative-dose protocol. Radiation Measurements. 32, 57–73.
919 Murray, A.S., Wintle, A.G., 2003. The single aliquot regenerative dose protocol: potential for
920 improvements in reliability. Radiation Measurements, 37, 377–381.
921 Nathan, R. P., Mauz, B., 2008. On the dose-rate estimate of carbonate-rich sediments for
922 trapped charge dating. Radiation Measurements. 43, 14-25.
923 Niespolo, E. M., Sharp, W.D., Avery, G., Dawson, T.E., 2021. Early, intensive marine resource
924 exploitation by Middle Stone Age humans at Ysterfontein 1 rockshelter, South Africa.
925 Proceedings of the National Academy of Sciences, 118,(16), 16 e2020042118
926 Parkington, J.E., 2001. Milestones: the impact of systematic exploitation of marine foods on
927 human evolution, in: Tobias, P.V., Raath, M.A., Moggi-Cechi, J., Doyle, G.A. (Eds.),
928 Humanity from African Naissance to Coming Millenia. Firenze University Press, Florence
929 pp. 327-336.
930 Parkington, J.E., 2003. Middens and moderns: shellfishing and the Middle Stone Age of the
931 Western Cape, South Africa. South African Journal of Science, 99, 243–247.
932 Parkington, J.E., 2010. Coastal diet, encephalization, and innovative behaviors in the late Middle
933 Stone Age of Southern Africa, in: Cunnane, S.C. Stewart, K.M. (Eds.), Human brain
934 evolution – the influence of freshwater and marine food resources. Wiley-Blackwell, New
935 Jersey, pp. 189–203.
936 Parkington, J.E., Poggenpoel, C., Halkett, D., Hart, T., 2004. Initial observations on the Middle
937 Stone Age coastal settlement in the Western Cape, South Africa, in: Conard, N.J. (Ed.)
938 Settlement dynamics of the Middle Paleolithic and Middle Stone Age Volume II. Kerns
939 Verlag, Tübingen, pp. 5-22.
940 Philippe, A., Guérin, G., Kreutzer, S., 2019. BayLum-An R package for Bayesian analysis of OSL
941 ages: an introduction. Quaternary Geochronology, 49, 16-24.
942 Prescott, J.R., Hutton, J.T., 1994. Cosmic ray contributions to dose rates for luminescence and
943 ESR dating: large depths and long-term time variations. Radiation Measurements. 23:
944 497–500.

945 Ramos, J., Bernal, D., Domınguez-Bella, S., Calado, D., Ruiz, B., Gil, M.J., Clemente, I.,Duran, J.J.,
946 Vijande, E., Chamorro, S., 2008. The Benzu rockshelter: a Middle Palaeolithic site on the
947 North African coast. Quaternary Science Reviews, 27, 2210-2218.
948 Ramos-Munoz, J., Cantillo-Duarte, J. J., Bernal-Casasola, D., Barrena-Tocino, A., Domínguez-
949 Bella, S., Vijande-Vila, E., Clemente-Conte, I., Gutierrez-Zugasti, I., Soriguer-Escofet, M.,
950 Almisas-Cruz, S., 2016. Early use of marine resources by Middle/Upper Pleistocene human
951 societies: the case of Benzú rockshelter (northern Africa). Quaternary International. 407,
952 16-28.
953 Richter, D., Richter, A. and Dornich, K., 2015. Lexsyg smart—a luminescence detection system
954 for dosimetry, material research and dating application. Geochronometria. 42(1), 202-
955 209.
956 Roberts, R.G., Galbraith, R.F., Yoshida, H., Laslett, G.M., Olley, J.M., 2000. Distinguishing dose
957 populations in sediment mixtures: a test of single-grain optical dating procedures using
958 mixtures of laboratory-dosed quartz. Radiation Measurements. 32(5-6), 459-465.
959 Rodnight, H., Duller, G.A.T., Wintle, A.G., Tooth, S., 2006. Assessing the reproducibility and
960 accuracy of optical dating of fluvial deposits. Quaternary Geochronology, 1(2), 109-120.
961 Schmid, V. C., Conard, N. J., Texier, P. J., Parkington, J. E., & Porraz, G. (2016). The 'MSA 1'of
962 Elands Bay Cave (South Africa) in the context of the southern African Early MSA
963 technologies. Southern African Humanities, 29(1), 153-201.
964 Steele, T.E., Alvarez-Fernández, E., 2011. Initial investigations into the exploitation of coastal
965 resources in North Africa during the late Pleistocene at Grotte Des Contrebandiers,
966 Morocco, in: Bicho, N., Haws, J.A., Davis, L.G. (Eds.), Trekking the shore: changing
967 coastlines and the antiquity of coastal settlement. Springer, New York, pp. 383-403.
968 Steele, T.E., Klein, R.G., 2013. The Middle and Later Stone Age faunal remains from Diepkloof
969 Rock Shelter, Western Cape, South Africa. Journal of Archaeological Science 40, 3453-
970 3462.
971 Steele, T.E., Mackay, A., Orton, J., Schwortz, S., 2016. Varsche Rivier 003, a new Middle Stone
972 Age site in southern Namaqualand, South Africa. The South African Archaeological
973 Bulletin. 67, 108-119.
974 Stoetzel, E., Campmas, E., Michel, P., Bougariane, B., Ouchaou, B., Amani, F., ElHajraoui, M.A.,
975 Nespoulet, R., 2014. Context of modern human occupations in North Africa: contribution
976 of the Témara caves data. Quaternary International. 320, 143-161.
977 Stringer, C., 2000. Coasting out of Africa. Nature, 405, 24–27.
978 Stringer, C.B., Finlayson, J.C., Barton, R.N., Fernández-Jalvo, Y., Cáceres, I., Sabin, R.C.,Rhodes,
979 E.J., Currant, A.P., Rodríguez-Vidal, J., Giles-Pacheco, F., Riquelme-Cantal, J.A., 2008.
980 Neanderthal exploitation of marine mammals in Gibraltar. Proceedings of the National
981 Academy of Sciences USA, 105, 14319-14324.
982 Thackeray, J.F., 1988. Molluscan fauna from Klasies River, South Africa. South African
983 Archaeological Bulletin. 43, 27–32.
984 Thomsen, K., Murray, A.S., Buylaert, J.P., Jain, M., Hansen, J.H., Aubry, T., 2016. Testing single-
985 grain quartz OSL methods using sediment samples with independent age control from
986 the Bordes-Fitterockshelter (Roches d'Abilly site, Central France). Quaternary
987 Geochronology. 31, 77–96.

Tribolo, C., Mercier, N., Rasse, M., Soriano, S., Huysecom, E., 2010. Kobo 1 and L'Abri-aux-Vaches (Mali, West Africa): two cases study for the optical dating of bioturbated sediments. Quaternary Geochronology. 5, 317-323.

Tribolo, C., Asrat, A., Bahain, J.-J., Chapon, C., Douville, E., Fragnol, C., Hernandez, M., Hovers, E., Leplongeon, A., Martin, L., Pleurdeau, D., Pearson, O., Puaud, S., Assefa, Z., 2017. When the Rains Stopped: Geochronological and Sedimentological Evidence for the Middle and Later Stone Age Sequence of Goda Buticha, Southeastern Ethiopia. PlosOne 12(1), e0169418.

Tribolo, C., 2020. Environnement, évolution comportementale et dynamique de peuplement en Afrique au cours du Middle Stone Age: approche géochronologique. Habilitation à diriger des recherches, Museum National d'Histoire Naturelle. 810 p.

Voigt, E., 1973. Stone Age molluscan utilization at Klasies River Mouth Caves. South African Journal of Science. 69, 306–309.

Volman, T.P., 1978. Early archaeological evidence for shellfish collecting. Science. 201, 911–913.

Volman, T.P., 1981. The Middle Stone Age in the southern Cape. Ph.D. Dissertation, University of Chicago.

Walter, R.C., Buffler, R.T., Bruggermann, J. H.,Guillauma, M.M.M., Berhe, S.M., Negassi, B.,Libsekal, Y., Cheng, H., Edwards, R.L., von Cosel, R., Néraudeau, D., Gagnon, M., 2000. Early human occupation of the Red Sea coast of Eritrea during the last interglacial. Nature. 405, 65–69.

Will, M., Parkington, J.E., Kandel, A.W., Conard, N.J., 2013. Coastal adaptations and the Middle Stone Age lithic assemblages from Hoedjiespunt 1 in the Western Cape, South Africa. Journal of Human Evolution. 64, 518–537.

Will, M., Kandel, A.W., Conard, N.J., 2015. Coastal adaptations and settlement systems on the Cape and Horn of Africa during the Middle Stone Age, in Conard, N.J., Delagnes, A. (Eds.), Settlement dynamics of the Middle Paleolithic and Middle Stone Age, Vol. IV. Kerns Verlag, Tübingen, pp. 61–89.

Will, M., Kandel, A.W., Kyriacou, K., Conard, N.J., 2016. An evolutionary perspective on coastal adaptations by modern humans during the Middle Stone Age of Africa. Quaternary International. 404, 68-86.

Will, M., Kandel, A. W., Conard, N. J., 2019. Midden or molehill: The role of coastal adaptations in human evolution and dispersal. Journal of World Prehistory. 32(1), 33-72.

Woodborne, S., 1999. Dating the Middle Stone Age in South Africa. National Research Foundation, Unpublished Final Report: 15/1/3/2/00231. Pretoria.

Woodborne, S., 2000. Luminescence dating of the Middle Stone Age in South Africa. National Science Foundation, Unpublished Report.

Zilhão, J., Angelucci, D., Badal, E., et al. (2010). Symbolic use of marine shells and mineral pigments by Iberian Neanderthals. Proceedings of the National Academy of Sciences of the United States of America, 107, 1023–1028.

Zilhão, J., Angelucci, D. E. , Araújo Igreja, M. , Arnold, L. J., Badal, E. , Callapez, P., Cardoso, J. L., d'Errico, F., Daura, J., Demuro, M., Deschamps, M., Dupont, C., Gabriel, S. D., Hoffmann, L., Legoinha, P., Matias, H., Monge Soares, A. M., Nabais, M., Portela, P. ,

Queffelec, A., Rodrigues, F. Souto. P., 2020. Last Interglacial Iberian Neandertals as Fisher-Hunter-Gatherers. Science, 367 (6485), eaaz7943.

Zimmerman, D.W., 1971. Thermoluminescent dating using fine grains from pottery. Archaeometry. 10, 26-28.